

AD-A124 079

HIGHER-ORDER COMPUTATIONAL METHODS FOR TRANSONIC  
WING/BODY FLOWFIELDS. (U) MCDONNELL DOUGLAS RESEARCH  
LABS ST LOUIS MO L T CHEN 30 SEP 82 MDC-Q0773  
DTNSRDC/ASED-CR-03-82 N00167-81-C-0057 F/G 1/3

1/1

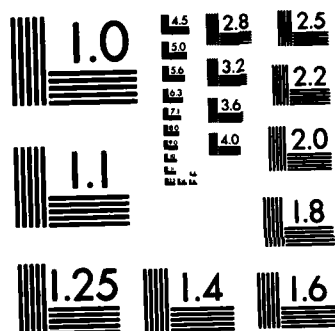
UNCLASSIFIED

NL

END

FILED

DTIC



MICROCOPY RESOLUTION TEST CHART  
NATIONAL BUREAU OF STANDARDS-1963-A

12

ADA 124 079

## HIGHER-ORDER COMPUTATIONAL METHODS FOR TRANSONIC WING/BODY FLOWFIELDS

L. T. Chen

McDonnell Douglas Research Laboratories  
St. Louis, Missouri 63166

30 September 1982

Final Report for Period 16 March 1981 - 30 September 1982

Approved for public release: distribution unlimited

David W. Taylor Naval Ship Research and Development Center  
Aviation and Surface Effects Department  
Bethesda, MD 20084

DTIC  
ELECTE  
S FEB 3 1983 D  
D

DTIC FILE COPY

88 02 02 013.

UNCLASSIFIED

SECURITY CLASSIFICATION OF THIS PAGE (When Data Entered)

REPORT DOCUMENTATION PAGE		READ INSTRUCTIONS BEFORE COMPLETING FORM
1. REPORT NUMBER DTNSRDC/ASED-CR-03-82	2. GOVT ACCESSION NO. AD-4124 579	3. RECIPIENT'S CATALOG NUMBER
4. TITLE (and Subtitle) Higher-Order Computational Methods for Transonic Wing/Body Flowfields		5. TYPE OF REPORT & PERIOD COVERED Final Report 16 Mar 81 - 30 Sep 82
		6. PERFORMING ORG. REPORT NUMBER Report MDC Q0773
7. AUTHOR(s) L. T. Chen		8. CONTRACT OR GRANT NUMBER(s) N00167-81-C-0057
9. PERFORMING ORGANIZATION NAME AND ADDRESS McDonnell Douglas Research Laboratories McDonnell Douglas Corporation St. Louis, MO 63166		10. PROGRAM ELEMENT, PROJECT, TASK AREA & WORK UNIT NUMBERS
11. CONTROLLING OFFICE NAME AND ADDRESS David W. Taylor Naval Ship Research and Development Center Bethesda, MD 20084		12. REPORT DATE 30 September 1982
14. MONITORING AGENCY NAME & ADDRESS (if different from Controlling Office)		13. NUMBER OF PAGES 53
		15. SECURITY CLASS. (of this report) Unclassified
15a. DECLASSIFICATION/DOWNGRADING SCHEDULE		
16. DISTRIBUTION STATEMENT (of this Report)  Approved for public release: distribution unlimited.		
17. DISTRIBUTION STATEMENT (of the abstract entered in Block 20, if different from Report)		
18. SUPPLEMENTARY NOTES		
19. KEY WORDS (Continue on reverse side if necessary and identify by block number) Transonic Wing-Body Flowfield Calculations Second- and Third-Order Numerical Methods Fully Conservative and Quasi-Conservative Formulations Partially Conservative Shock-Point Operators		
20. ABSTRACT (Continue on reverse side if necessary and identify by block number) → This report presents the development of higher-order finite-difference schemes for application to transonic wing-body flow calculations. These schemes treat supersonic flows and shocks more accurately than most existing schemes. A transformed full potential equation in a general curvilinear coordinate system is derived, and higher-order operators are introduced. A new shock-point operator produces Mach number jumps at a shock that agree reasonably well with Rankine-Hugoniot values. Second- and third-order, quasi-conservative, and		

UNCLASSIFIED

SECURITY CLASSIFICATION OF THIS PAGE(When Data Entered)

fully conservative schemes are thereby developed for general geometries where flow directions can be approximately aligned with coordinate lines in supersonic regions. The fully conservative schemes are developed by modifying an existing finite-volume algorithm, while the quasi-conservative schemes are developed by solving the transformed full potential equation directly with the addition of the second- and third-order artificial viscosities at supersonic points, and the corresponding first- and second-order shock-point operators at shock points.

To evaluate the proposed shock-point operators, a model problem was studied, consisting of flow through a converging-diverging planar channel, with a shock in the diverging section. The computed shock locations and strengths were compared with a one-dimensional analysis including Rankine-Hugoniot shocks. These methods were successfully extended to three-dimensional flowfield computations. Computed results are presented for an ONERA-M6 wing on a vertical wall and on a semi-infinite fuselage and compared with corresponding experimental data.

UNCLASSIFIED

SECURITY CLASSIFICATION OF THIS PAGE(When Data Entered)

## PREFACE

This final report is an account of the work completed at the McDonnell Douglas Research Laboratories (MDRL) on Higher-Order Computational Methods for Transonic Wing/Body Flowfields, Contract No. N00167-81-C-0057, from 16 March 1981 to 30 September 1982, supported by the Naval Air System Command (320D) under the cognizances of D. G. Kirkpatrick. The work was done in the Flight Sciences Department, managed by Dr. R. J. Hakkinen. The principal investigator was Dr. L. T. Chen. The program monitor was Dr. T. C. Tai, David W. Taylor Naval Ship Research and Development Center.

*R. J. Hakkinen*

R. J. Hakkinen

Director-Research, Flight Sciences

McDonnell Douglas Research Laboratories

*D. P. Ames*

D. P. Ames

Staff Vice President

McDonnell Douglas Research Laboratories

Accession For	
NTIS GRA&I	<input checked="checked" type="checkbox"/>
DTIC TAB	<input type="checkbox"/>
Unannounced	<input type="checkbox"/>
Justification	
By _____	
Distribution/ _____	
Availability Codes	
Dist	Avail and/or Special
A	



## CONTENTS

	<u>Page</u>
1. INTRODUCTION.....	1
2. NOMENCLATURE.....	3
3. FULL POTENTIAL EQUATION.....	4
4. SUPERSONIC FLOW AND SHOCKS.....	10
4.1 Artificial Viscosities and Partially Conservative Shock-Point Operators.....	11
4.2 A Simple One-Dimensional Flow Analysis and a Shock- Point Operator.....	13
4.3 Relaxation Strategies.....	15
5. ANALYSIS OF SHOCKS IN CHANNEL FLOWS.....	17
6. WING-BODY FLOWFIELD COMPUTATION.....	32
6.1 Grid Generation and Computational Domain.....	32
6.2 Boundary Conditions.....	33
6.3 Numerical Results.....	35
7. CONCLUSIONS.....	43
ACKNOWLEDGMENT.....	44
REFERENCES.....	45

# LIST OF ILLUSTRATIONS

	<u>Page</u>
Figure 1 Transformation of a second-order element.....	9
Figure 2 A converging-diverging channel.....	17
Figure 3 Grid distribution about channel-C.....	18
Figure 4 Comparison of computed average shock Mach number with analytical solutions.....	21
Figure 5 Comparison of computed stagnation density changes across shocks with analytical solutions.....	22
Figure 6 Mach number distribution for channel flow of case 3.....	23
Figure 7 Mach number distribution for channel flow of case 7.....	24
Figure 8 Mach number distribution for channel flow of case 12....	25
Figure 9 Mach number distribution for channel flow of case 13....	26
Figure 10 Mach number distribution for channel flow of case 15....	27
Figure 11 Mach number distribution for channel flow of case 18....	28
Figure 12 Mach number distribution for channel flow of case 20....	29
Figure 13 Mach number distribution for channel flow of case 23....	30
Figure 14 Mach number distribution for channel flow of case 26....	31
Figure 15 Physical and computational domains for a wing-fuselage configuration.....	32
Figure 16 Grid distribution on an ONERA-M6 wing and a vertical wall.....	33
Figure 17 Grid distribution on an ONERA-M6 wing and a semi-infinite fuselage.....	33
Figure 18 Comparison of first- and second-order fully conservative solutions.....	36
Figure 19 Comparison of first- and second-order fully conservative solutions.....	36
Figure 20 Pressure distributions on the upper and lower surfaces of an ONERA-M6 wing on a wall at the 20% semi-span location.....	37
Figure 21 Pressure distributions on the upper and lower surfaces of an ONERA-M6 wing on a wall at the 65% semi-span location.....	38



# LIST OF ILLUSTRATIONS (Concluded)

	<u>Page</u>
Figure 22 Pressure distributions on the upper and lower surfaces of an ONERA-M6 wing on a wall at the 95% semi-span location.....	38
Figure 23 Comparison of third-order quasi-conservative and fully conservative solutions at the 65% semi-span location....	39
Figure 24 Comparison of third-order quasi-conservative and fully conservative solutions at the 95% semi-span location....	39
Figure 25 Study of partially conservative shock-point operators at 20% semi-span location on an ONERA-M6 wing.....	41
Figure 26 Study of partially conservative shock-point operators at 65% semi-span location on an ONERA-M6 wing.....	42
 Table 1 Summary of channel flow calculations.....	 19

## 1. INTRODUCTION

Most existing schemes<sup>1-5</sup> for computing transonic potential flowfields about wings or wing-body combinations are limited to first-order accuracy in supersonic regions because of the use of first-order upwind differencing or the addition of first-order artificial viscosities or densities. Although these schemes have been used extensively for preliminary aerodynamic design, most of their successful applications are limited to simple wing-body geometries. Extension to more complex geometries is prohibited by the need for a large number of grid points for adequate prediction of shock location and strength, especially in the case of double shocks which are common features of flow about highly swept and aft-cambered wings. Development of higher-order schemes is therefore necessary to improve the resolution of solutions, with a reasonable number of grid points, for realistic wing-body geometries.

Several second-order schemes<sup>6-9</sup> have been introduced for airfoil and cascade flowfield calculations. Jameson<sup>10</sup> and Chen<sup>7</sup> demonstrated that second-order fully conservative and quasi-conservative schemes, respectively, are capable of predicting double shocks on an airfoil surface, which cannot be accurately resolved using a first-order scheme without a large number of grid points. Chen<sup>7</sup> also demonstrated that his second-order quasi-conservative scheme provides better resolution of a double shock than the second-order fully conservative scheme. Ives and Liutermoza<sup>8</sup> showed that their second-order nonconservative scheme provides better resolution for transonic cascade flows than first-order nonconservative schemes. A discussion of first- and second-order nonconservative schemes has also been given in Reference 7. A study of artificial viscosities and conservative shock-point operators of different orders was provided by Chen and Caughey,<sup>11</sup> who also introduced a third-order quasi-conservative scheme. In the present study, second- and third-order artificial viscosities are first introduced for transonic potential flowfield computations about wings and wing-body combinations.

Methods for differencing the small disturbance equation at shocks were investigated by Murman<sup>12</sup> and Hafez.<sup>13</sup> Methods for treating shocks in a full potential formulation were studied by Jameson<sup>14</sup> and Chen and Caughey.<sup>11</sup> Fully conservative schemes for treating the potential equation conserve mass flux

isentropically across shocks; therefore, the predicted shocks are always stronger than Rankine-Hugoniot shocks.<sup>2</sup> In the present study, a shock-point operator is derived from an approximate one-dimensional flow analysis. Use of this operator results in Mach number jumps at shocks which are in reasonable agreement with Rankine-Hugoniot values. Methods for differencing at shocks are evaluated using a model problem consisting of flow through a converging-diverging planar channel, with a shock in the diverging section. In flowfield calculations about wings, partially conservative shock-point operators provide results that are in better agreement with experiment than a conservative scheme. To the author's knowledge, this result is 1) the first demonstration of a successful third-order scheme applied to solution of the full potential equation, 2) first presentation of both second- and third-order solutions for transonic potential flowfield computations about wings and wing-body configurations, and 3) first demonstration of a shock-point operator that produces Mach number jumps in a potential flow which are in reasonable agreement with Rankine-Hugoniot values.

## 2. NOMENCLATURE

$a$	speed of sound
$a_0$	stagnation speed of sound
$a_*$	speed of sound at $M = 1$
$\tilde{A} \tilde{B} \tilde{C}$	transformation matrices defined in Equations (3), (4), and (5)
$c_1, c_2 \dots c_9$	coefficients defined in Equations (9)-(17) and also Equations (38)-(42)
$D$	determinant of Jacobian transformation matrix defined in Equations (33) and (47)
$G$	reduced velocity potential defined in Equation (69)
$h_1, h_2 \dots h_9$	coefficients defined in Equations (21)-(29)
$H$	artificial viscosities at supersonic points defined in Equations (53) and (56)
$H_s$	artificial viscosities at shock points defined in Equations (55) and (57)
$\dot{m}$	mass flow rate defined in Equation (68)
$M$	local Mach number
$M^*$	normalized Mach number $= u/a_*$
$P_m$	partially conservative parameter defined in Equations (55) and (57)
$P_x, P_y, P_z$	second-order transformation derivatives defined in Equations (30)-(32) and (48)-(49)
$s$	coordinate in streamwise direction
$u, v, w$	velocity component in $x, y$ , and $z$ directions defined in Equations (34)-(36)
$U, V, W$	velocity components defined in Equations (18)-(20)
$x, y, z$	coordinates in physical space
$x_s$	location of shock in the channel axis
$\mu$	switch function defined in Equation (54)
$\rho$	local flow density
$\rho^*$	flow density at $M = 1$

### 3. FULL POTENTIAL EQUATION

Quasi-conservative schemes are used to solve finite-difference approximations of the full potential equation. Therefore, it is convenient to first formulate the full potential equation in computational coordinates. By applying the chain rule, derivatives of the potential function  $\phi$  in physical coordinates  $(x, y, z)$  can be related to its derivatives in an arbitrary curvilinear coordinate system  $(X, Y, Z)$  as follows:

$$\begin{bmatrix} \phi_x \\ \phi_y \\ \phi_z \end{bmatrix} = \underline{\underline{A}} \begin{bmatrix} \phi_X \\ \phi_Y \\ \phi_Z \end{bmatrix} \quad (1)$$

$$\begin{bmatrix} \phi_{xx} \\ \phi_{yy} \\ \phi_{xy} \\ \phi_{zz} \\ \phi_{xz} \\ \phi_{yz} \end{bmatrix} = - \underline{\underline{B}} \underline{\underline{C}} \underline{\underline{A}} \begin{bmatrix} \phi_X \\ \phi_Y \\ \phi_Z \end{bmatrix} + \underline{\underline{B}} \begin{bmatrix} \phi_{XX} \\ \phi_{YY} \\ \phi_{XY} \\ \phi_{ZZ} \\ \phi_{XZ} \\ \phi_{YZ} \end{bmatrix}, \quad (2)$$

where

$$\underline{\underline{A}} = \begin{bmatrix} x_X & y_X & z_X \\ x_Y & y_Y & z_Y \\ x_Z & y_Z & z_Z \end{bmatrix}^{-1} \quad (3)$$

$$\tilde{B} = \begin{bmatrix} x_X^2 & y_X^2 & 2x_X y_X & z_X^2 & 2x_X z_X & 2y_X z_X \\ x_Y^2 & y_Y^2 & 2x_Y y_Y & z_Y^2 & 2x_Y z_Y & 2y_Y z_Y \\ x_X x_Y & y_X y_Y & x_X y_Y + x_Y y_X & z_X z_Y & x_X z_Y + x_Y z_X & y_X z_Y + y_Y z_X \\ x_Z^2 & y_Z^2 & 2x_Z y_Z & z_Z^2 & 2x_Z z_Z & 2y_Z z_Z \\ x_X x_Z & y_X y_Z & x_X y_Z + x_Z y_X & z_X z_Z & x_X z_Z + x_Z z_X & y_X z_Z + y_Z z_X \\ x_Y x_Z & y_Y y_Z & x_Y y_Z + x_Z y_Y & z_Y z_Z & x_Y z_Z + x_Z z_Y & y_Y z_Z + y_Z z_Y \end{bmatrix}^{-1}, \quad (4)$$

and

$$\tilde{C} = \begin{bmatrix} x_{XX} & x_{YY} & x_{XY} & x_{ZZ} & x_{XZ} & x_{YZ} \\ y_{XX} & y_{YY} & y_{XY} & y_{ZZ} & y_{XZ} & y_{YZ} \\ z_{XX} & z_{YY} & z_{XY} & z_{ZZ} & z_{XZ} & z_{YZ} \end{bmatrix}^T. \quad (5)$$

The full potential equation to be solved is

$$(a^2 - u^2)\phi_{xx} + (a^2 - v^2)\phi_{yy} + (a^2 - w^2)\phi_{zz} - 2uv\phi_{xy} - 2vw\phi_{yz} - 2uw\phi_{xz} = 0, \quad (6)$$

where  $u, v, w$  are the  $x, y, z$  components of the flow velocity, respectively, and  $a$  is the local speed of sound determined from the energy equation

$$a^2 = a_0^2 - \frac{\gamma - 1}{2} (u^2 + v^2 + w^2), \quad (7)$$

where  $\gamma$  is the ratio of specific heats for the assumed calorically perfect gas and  $a_0$  is the stagnation speed of sound.

Substituting Equations (1) and (2) into Equation (6), and after performing matrix inversion, multiplication, and careful algebraic manipulation, a

full potential equation multiplied by the determinant of the Jacobian transformation matrix,  $D$ , in arbitrary curvilinear coordinates can be derived as

$$c_1\phi_{XX} + c_2\phi_{YY} + c_3\phi_{ZZ} + c_4\phi_{XY} + c_5\phi_{YZ} + c_6\phi_{XZ} \\ + c_7\phi_X + c_8\phi_Y + c_9\phi_Z = 0, \quad (8)$$

where

$$c_1 = [a^2(h_1^2 + h_2^2 + h_3^2) - U^2]/D \quad (9)$$

$$c_2 = [a^2(h_4^2 + h_5^2 + h_6^2) - V^2]/D \quad (10)$$

$$c_3 = [a^2(h_7^2 + h_8^2 + h_9^2) - W^2]/D \quad (11)$$

$$c_4 = [2a^2(h_1h_4 + h_2h_5 + h_3h_6) - 2UV]/D \quad (12)$$

$$c_5 = [2a^2(h_4h_7 + h_5h_8 + h_6h_9) - 2VW]/D \quad (13)$$

$$c_6 = [2a^2(h_1h_7 + h_2h_8 + h_3h_9) - 2UW]/D \quad (14)$$

$$c_7 = (h_1p_X + h_2p_Y + h_3p_Z)/D \quad (15)$$

$$c_8 = (h_4p_X + h_5p_Y + h_6p_Z)/D \quad (16)$$

$$c_9 = (h_7p_X + h_8p_Y + h_9p_Z)/D, \quad (17)$$

$U, V, W$  are velocity components defined as

$$U = h_1u + h_2v + h_3w \quad (18)$$

$$V = h_4u + h_5v + h_6w \quad (19)$$

$$W = h_7u + h_8v + h_9w, \quad (20)$$

coefficients  $h_1, h_2, \dots, h_9$  are first-order transformation derivatives defined as

$$h_1 = y_Y z_Z - y_Z z_Y \quad (21)$$

$$h_2 = z_Y x_Z - z_Z x_Y \quad (22)$$

$$h_3 = x_Y y_Z - x_Z y_Y \quad (23)$$

$$h_4 = y_Z z_X - y_X z_Z \quad (24)$$

$$h_5 = z_Z x_X - z_X x_Z \quad (25)$$

$$h_6 = x_Z y_X - x_X y_Z \quad (26)$$

$$h_7 = y_X z_Y - y_Y z_X \quad (27)$$

$$h_8 = z_X x_Y - z_Y x_X \quad (28)$$

$$h_9 = z_X y_Y - x_Y y_X , \quad (29)$$

and coefficients  $p_X$ ,  $p_Y$ , and  $p_Z$  are second-order transformation derivatives defined as

$$p_X = c_1^{x_{XX}} + c_2^{x_{YY}} + c_3^{x_{ZZ}} + c_4^{x_{XY}} + c_5^{x_{YZ}} + c_6^{x_{XZ}} \quad (30)$$

$$p_Y = c_1^{y_{XX}} + c_2^{y_{YY}} + c_3^{y_{ZZ}} + c_4^{y_{XY}} + c_5^{y_{YZ}} + c_6^{y_{XZ}} \quad (31)$$

$$p_Z = c_1^{z_{XX}} + c_2^{z_{YY}} + c_3^{z_{ZZ}} + c_4^{z_{XY}} + c_5^{z_{YZ}} + c_6^{z_{XZ}} . \quad (32)$$

The determinant of the Jacobian transformation matrix is defined as

$$D = h_1 x_X + h_4 x_Y + h_7 x_Z . \quad (33)$$

The velocity components  $u$ ,  $v$ ,  $w$  are defined as

$$u = (h_1 \phi_X + h_4 \phi_Y + h_7 \phi_Z) / D \quad (34)$$

$$v = (h_2 \phi_X + h_5 \phi_Y + h_8 \phi_Z) / D \quad (35)$$



$$w = (h_3\phi_X + h_6\phi_Y + h_9\phi_Z)/D. \quad (36)$$

Equation (8) can be reduced to a two-dimensional equation:

$$c_1\phi_{XX} + c_2\phi_{YY} + c_4\phi_{XY} + c_7\phi_X + c_8\phi_Y = 0, \quad (37)$$

where  $c_1$ ,  $c_2$ ,  $c_4$ ,  $c_7$ , and  $c_8$  reduce to

$$c_1 = [a^2(x_Y^2 + y_Y^2) - U^2]/D^2 \quad (38)$$

$$c_2 = [a^2(x_X^2 + y_X^2) - V^2]/D^2 \quad (39)$$

$$c_4 = -2[a^2(x_Xx_Y + y_Xy_Y) - UV]/D^2 \quad (40)$$

$$c_7 = (x_Yp_Y - y_Yp_X)/D \quad (41)$$

$$c_8 = (y_Xp_X - x_Xp_Y)/D \quad (42)$$

and  $U$ ,  $V$ ,  $u$ ,  $v$ ,  $J$ ,  $D$ ,  $p_X$ , and  $p_Y$  are redefined as

$$U = uy_Y - vx_Y \quad (43)$$

$$V = uy_X - vx_X \quad (44)$$

$$u = (y_Y\phi_X - y_X\phi_Y)/D \quad (45)$$

$$v = (x_X\phi_Y - x_Y\phi_X)/D \quad (46)$$

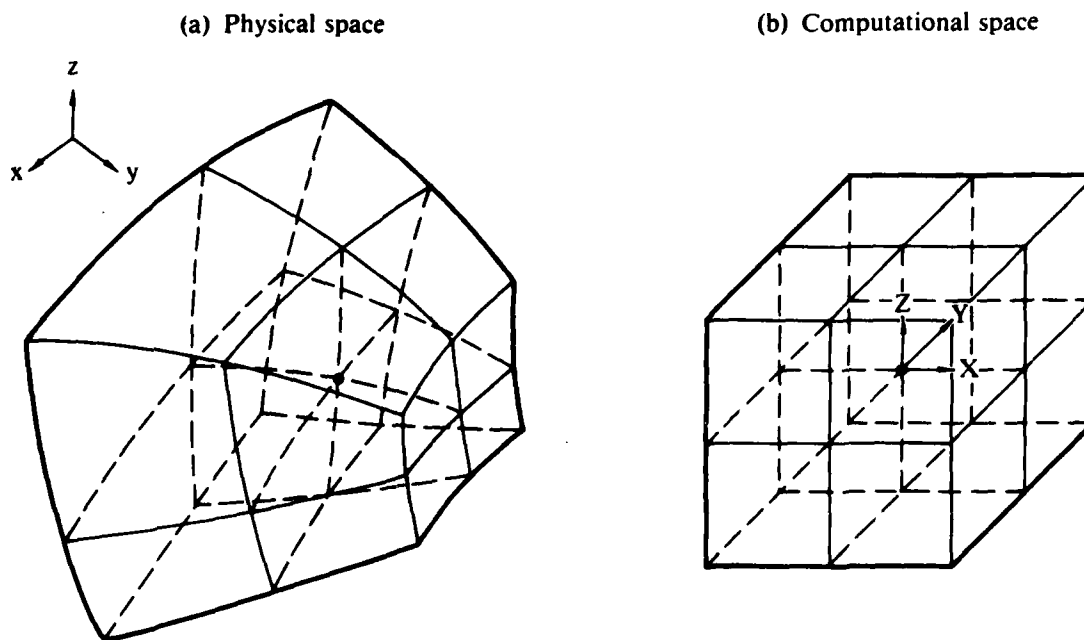
$$D = x_Xy_Y - x_Yy_X \quad (47)$$

$$p_X = c_1x_{XX} + c_2x_{YY} + c_3x_{XY} \quad (48)$$

$$p_Y = c_1y_{XX} + c_2y_{YY} + c_3y_{XY}. \quad (49)$$

Equation (37) is consistent with the two-dimensional equation derived in Reference 7.

After the physical coordinates of grid points have been prescribed, the transformation derivatives  $x_X, x_Y, x_Z, y_X, \dots, x_{XX}, x_{XY}, x_{YY}, \dots$  can be computed at each control point within a local mesh element. A second-order-accurate, finite-difference approximation of the transformed full potential equation thus can be obtained by applying a second-order element (Figure 1). Within the element,  $X, Y,$  and  $Z$  vary from  $-1$  to  $1$  from nodal point to nodal point. Therefore the mesh element is uniformly spaced in the computational space. Second-order shape functions can be constructed that relate the function at any point  $p$  within the element to the values of the function at 27 nodal points. If the control point is chosen to be  $X = Y = Z = 0$ , then the well-known second-order, centered, finite-difference formulations<sup>15,16</sup> are obtained.



GP21-0803-15

Figure 1. Transformation of a second-order element.

#### 4. LOCAL SUPERSONIC FLOW AND SHOCKS

The finite-difference approximation to the full potential equation discussed thus far is adequate for flows that are entirely subsonic. To treat transonic flows, proper artificial viscosities or densities are normally added to the finite-difference approximation of the potential equation solved at supersonic points. The directional bias of supersonic flows thus can be reflected in the governing equation.

The so-called fully conservative and quasi-conservative schemes conserve the artificial viscosities or densities along streamlines; in other words, the total summation of artificial viscosities or densities added to the potential equation at all points along the streamline is exactly zero. Naturally the shocks thus predicted are consistent with isentropic mass-conserving shocks, which do not simultaneously conserve momentum and therefore are stronger than the Rankine-Hugoniot shocks. However, in the nonconservative schemes, the total summation of artificial viscosities or densities added along the streamline is not zero. In the limit of the finite-difference approximation, this unbalanced summation term appears as a nonzero source term on the right side of the potential equation solved at certain points along the streamline generally at the shock point, the first subsonic point downstream of the shock. This source term in the equation represents a mass source in the flowfield. Therefore, the solutions thus obtained deviate from the isentropic mass-conserving solutions.

Since the potential formulation does not permit simultaneous conservation of mass and momentum flux at shocks, errors in the jumps in fluid properties are inevitable. A desirable method from an engineering point of view is one in which errors in the properties of primary interest are minimized. As a matter of fact, it has been consistently shown that the shocks computed by these nonconservative schemes agree better with experiment than those computed by the conservative schemes.<sup>17</sup> The nature of the nonzero source term was understood to be related to the addition of mass flux; however, an adequate mathematical explanation of its effect has not been given. An attempt to explain the nonzero source term will be given in Section 4.2, in the form of a simple one-dimensional flow analysis, following the introduction of artificial viscosities in Section 4.1.

#### 4.1 Artificial Viscosities and Partially Conservative Shock Point Operators

The second derivative of the potential function in the streamwise direction,  $s$ , is given as

$$\phi_{ss} = \frac{a^2}{q^2} (u^2 \phi_{xx} + v^2 \phi_{yy} + w^2 \phi_{zz} + 2uv \phi_{xy} + 2vw \phi_{yz} + 2uw \phi_{xz}) . \quad (50)$$

Substituting Equations (1) and (2) into Equation (50) yields

$$\phi_{ss} = \frac{1}{q^2} (U^2 \phi_{XX} + V^2 \phi_{YY} + W^2 \phi_{ZZ} + 2UV \phi_{XY} + 2VW \phi_{YZ} + 2UW \phi_{XZ}) , \quad (51)$$

where  $U, V, W$  are given in Equations (18)-(20).

The directional bias of supersonic flows can be properly simulated by performing an upwind differencing or adding artificial viscosities in the approximate streamwise direction. If  $Y = \text{constant}$  lines are in the approximate  $s$  direction, the principal part of  $\phi_{ss}$  can be approximated by

$$\phi_{ss} = \frac{U^2}{q^2} \phi_{XX} . \quad (52)$$

A second-order artificial viscosity can be expressed as

$$H = (\Delta X)^2 \left[ \frac{\mu U^2 \phi_{XX}}{D} \right]_{XX} = \left( \frac{\mu U^2 \phi_{XX}}{D} \right)_{i-2} - 2 \left( \frac{\mu U^2 \phi_{XX}}{D} \right)_{i-1} + \left( \frac{\mu U^2 \phi_{XX}}{D} \right)_1 , \quad (53)$$

where

$$\mu = \max \left( 1 - \frac{a^2}{q^2} , 0 \right) . \quad (54)$$

$H$  is then added to the finite-difference representation of Equation (8) at supersonic points. At shock points, i.e., the first downstream subsonic points after the shocks, the following first-order artificial viscosity  $H_s$  is added with  $p_m$  controlling the nonconservative differencing:

$$H_s = (p_m - 1) \left[ \frac{(\Delta X) \mu U^2 \phi_{XX}}{D} \right]_X = \left[ \left( \frac{\mu U^2 \phi_{XX}}{D} \right)_{i-1} - \left( \frac{\mu U^2 \phi_{XX}}{D} \right)_{i-2} \right] (p_m - 1). \quad (55)$$

If  $p_m = 0$ , the quantity  $\mu U^2 \phi_{XX}$  is conserved along  $Y = \text{constant}$  lines, implying that the added artificial viscosities are conserved along approximate streamlines. If  $p_m > 0$ , a numerical mass flux is introduced at shocks, modifying the locations and strengths of the shocks. The effect of  $p_m$  on the captured shocks will be discussed later. Although  $\mu$  is a ramp function, both  $H$  and  $H_s$  reduce to zero as the mesh size goes to zero. The solution is second-order accurate at both subsonic and supersonic points, and first-order accurate at shock points. The scheme is second-order quasi-conservative. In the so-called quasi-conservative schemes, only the differencing of artificial viscosities is in divergence form; the differencing of the governing potential equation is not. A second-order fully conservative scheme also can be constructed by incorporating  $H$  and  $H_s$  into the existing finite-volume algorithm.

Third-order, quasi-conservative and fully conservative schemes can be developed by adding the following third-order artificial viscosity at supersonic points:

$$H = \left[ \frac{(\Delta X)^3 \mu U^2 \phi_{XX}}{D} \right]_{XXX} = \left( \frac{\mu U^2 \phi_{XX}}{D} \right)_i - 3 \left( \frac{\mu U^2 \phi_{XX}}{D} \right)_{i-1} + 3 \left( \frac{\mu U^2 \phi_{XX}}{D} \right)_{i-2} - \left( \frac{\mu U^2 \phi_{XX}}{D} \right)_{i-3} \quad (56)$$

and adding the following second-order artificial viscosity at shock points:

$$H_s = (p_m - 1) \left[ \frac{(\Delta X)^3 \mu U^2 \phi_{XX}}{D} \right]_{XX} = \left[ \left( \frac{\mu U^2 \phi_{XX}}{D} \right)_{i-3} - 2 \left( \frac{\mu U^2 \phi_{XX}}{D} \right)_{i-2} + \left( \frac{\mu U^2 \phi_{XX}}{D} \right)_{i-1} \right] (p_m - 1). \quad (57)$$

If  $p_m$  is set to zero, the quantity  $\mu U^2 \phi_{XX}$  is conserved along  $Y = \text{constant}$  lines. If  $p_m$  is set to be greater than zero, a numerical mass flux is added at shocks, as in the second-order schemes.

#### 4.2 A Simple One-Dimensional Flow Analysis and a Shock-Point Operator

An alternative new method to formulate a shock-point operator is described in the following paragraphs. This method is based on an approximate one-dimensional analysis in which information from the Rankine-Hugoniot relations is incorporated.

The flows upstream and downstream of the shock can be considered as relating to two branches of isentropic flows. Because of the entropy increase across the shock, the stagnation density decreases, while the stagnation speed of sound remains unchanged because the process is adiabatic. The continuity equation can therefore be written as

$$\rho_1^* M_1 \left(1 + \frac{\gamma - 1}{2} M_1^2\right)^{-3} = \rho_2^* M_2 \left(1 + \frac{\gamma - 1}{2} M_2^2\right)^{-3} \quad (58)$$

or

$$\int_{x_1}^{x_2} [\rho^* M \left(1 + \frac{\gamma - 1}{2} M^2\right)]_x dx = 0, \quad (59)$$

where  $x_1$  and  $x_2$  are the axial positions just upstream and downstream of the shock and  $\rho_1^*$ ,  $\rho_2^*$ ,  $M_1$  and  $M_2$  are sonic densities and Mach numbers of the flows just upstream and downstream of the shock. If the Mach number is assumed to change smoothly across the shock, as occurs in most finite-difference solutions, the integration followed by the differentiation of the term inside the bracket can be performed to give the following approximate equation.

$$(1 - M^{*2})(M_2^* - M_1^*) = - \left(1 - \frac{\gamma - 1}{\gamma + 1} M^{*2}\right) M^* \left(1 - \frac{\rho_2^*}{\rho_1^*}\right), \quad (60)$$

where  $M^* = u/a_* = \phi_x/a_*$  and  $a_*$  is the sonic speed at  $M = 1$ . Two approximations have been made: the  $(1 - M^{*2})$  term on the left side and the  $[1 - (\gamma - 1)/(\gamma + 1)M^{*2}]M^*$  term on the right side are treated as constants during integration, and the relative change in  $\rho^*$  is assumed to be small. In a fully isentropic flow,  $\rho^*$  is constant; the right side of Equation (60) is therefore zero, and the left side can be rewritten as the familiar one-dimensional potential equation

$$(a^2 - u^2)\phi_{xx} = 0. \quad (61)$$

A change in  $\rho^*$  occurs across a shock in a real flow. The right side of Equation (60) should be related to the error incurred at a shock in a potential flow calculation.  $M^*$  on the right side of Equation (60) is the average value of  $M_1^*$  and  $M_2^*$ , and therefore a reasonable approximation is  $M^* = 1$ . If this approximation is made, and the left side notation of Equation (61) is retained for clarity,

$$(a^2 - u^2)\phi_{xx} = -a_*^3 \left(1 - \frac{\rho_2^*}{\rho_1^*}\right) / \Delta x, \quad (62)$$

where  $\Delta x$  is the axial spacing across the shock. Numerical values for the right side of Equation (62) can be obtained by introducing a Rankine-Hugoniot relation,

$$\frac{\rho_2^*}{\rho_1^*} = M_1^{*\frac{2\gamma}{\gamma-1}} \left\{ \frac{1 - \frac{\gamma-1}{\gamma+1} M_1^{*2}}{M_1^{*2} - \frac{\gamma-1}{\gamma+1}} \right\}^{\frac{1}{\gamma-1}}, \quad (63)$$

where  $\rho_1^*$  and  $\rho_2^*$  are values of  $\rho^*$  upstream and downstream of shocks, respectively, and  $M_1^*$  is the normalized shock Mach number upstream of the shock.

This result is used to modify the conservative first- and second-order artificial viscosities at shock points as follows (see Equations (55) and (57)):

$$H_s = - \left[ \frac{(\Delta X) \mu U^2 \phi_{XX}}{D} \right]_X + a_*^3 \left( 1 - \frac{\rho_2^*}{\rho_1^*} \right) / \Delta x_s \quad (64)$$

and

$$H_s = - \left[ \frac{(\Delta X)^3 \mu U^2 \phi_{XX}}{D} \right]_{XX} + a_*^3 \left( 1 - \frac{\rho_2^*}{\rho_1^*} \right) / \Delta x_s, \quad (65)$$

where  $\Delta x_s$  is the distance between the shock point and its upstream supersonic point in the streamwise direction.

#### 4.3 Relaxation Strategies

The finite-difference approximation to Equation (8) can be solved by a line-relaxation scheme with the boundary conditions described in the previous section. To ensure that the relaxation scheme corresponds to a convergent process, the old and updated values of the potential function,  $\phi$  and  $\phi^+$ , must be mixed properly. The basic relaxation strategies developed for the present method are similar to the ones described in References 15 and 18, except for careful treatment of artificial viscosities at supersonic and shock points.

In the second-order quasi-conservative scheme, the old and new values of  $\phi$  contributing to the terms  $(q^2 - a^2)\phi_{ss} + H$  (or  $H_s$ ) of the relaxation equation are chosen to ensure a convergent process in the  $i = \text{constant}$  line sweep according to

$$\begin{aligned} (q^2 - a^2) \phi_{ss} + H = & \left[ \left( \frac{\mu U^2}{D} \right)_{i,j,k} + 4 \left( \frac{\mu U^2}{D} \right)_{i-m,j,k} + \left( \frac{\mu U^2}{D} \right)_{i-2m,j,k} \right] \\ & \times (c_{i,j,k} - c_{i-m,j,k}) - 2 \left[ \left( \frac{\mu U^2}{D} \right)_{i-m,j,k} + \left( \frac{\mu U^2}{D} \right)_{i-2m,j,k} \right] \\ & \times (c_{i,j,k} - c_{i-2m,j,k}) + R_{ss} \end{aligned} \quad (66)$$



for supersonic points, and

$$\begin{aligned}
 (q^2 - a^2) \phi_{ss} + H_s = & 2 \left[ \left( \frac{\mu U^2}{D} \right)_{i-m,j,k} + \left( \frac{\mu U^2}{D} \right)_{i-2m,j,k} \right] (1 - p_m) \\
 & \times (c_{i,j,k} - c_{i-m,j,k}) - \left[ \left( \frac{\mu U^2}{D} \right)_{i-m,j,k} - 2 \left( \frac{\mu U^2}{D} \right)_{i-2m,j,k} \right] \\
 & \times (1 - p_m) (c_{i,j,k} - c_{i-2m,j,k}) + R_{ss}
 \end{aligned} \tag{67}$$

for shock points, where  $c_{i,j,k} = \phi_{i,j,k}^+ - \phi_{i,j,k}$  is the correction to the potential function,  $m$  is equal to 1 or -1 if  $U > 0$  or  $U < 0$ , respectively, and  $R_{ss}$  is the residual of the finite-difference approximation to  $(q^2 - a^2)\phi_{ss}$  evaluated using old values of  $\phi$ . The second-order fully conservative scheme applies the same strategy to treat the artificial viscosities at supersonic and shock points. A similar strategy also can be developed for the third-order quasi-conservative and fully conservative schemes.

## 5. ANALYSIS OF SHOCKS IN CHANNEL FLOWS

A model problem, consisting of flow through a planar, symmetric converging-diverging channel (Figure 2) was used to evaluate various methods for treatment of shock waves in potential flow. This configuration provides a relatively simple, inexpensive framework for evaluation of numerical methods, prior to incorporation into a three-dimensional method.

The flow becomes sonic at the throat,  $x_t$ , and shocks occur in the diverging section extending from  $x_t$  to  $x_e$ . The slope of the diverging wall can be adjusted so that the predicted shock Mach numbers range from 1.0 to 2.0. Values of  $p_m$  vary from -0.6 to 0.8, and mass flux across each  $x$  station is computed to check the mass flux conservation.

A previously developed inlet program<sup>15</sup> was modified to compute the flows with shocks in the channel by incorporating the second- and third-order artificial viscosities and the partially conservative shock-point operators described previously. A typical grid system is presented in Figure 3. In the calculation, two meshes were used; the coarse mesh had 50 mesh elements in the unwrapped X-direction, 12 mesh elements in the surface normal direction, and 20 equally spaced streamwise mesh elements in the diverging section. The fine mesh had twice as many mesh elements in both directions. To ensure that a converged solution in the fine mesh existed and to improve the convergence

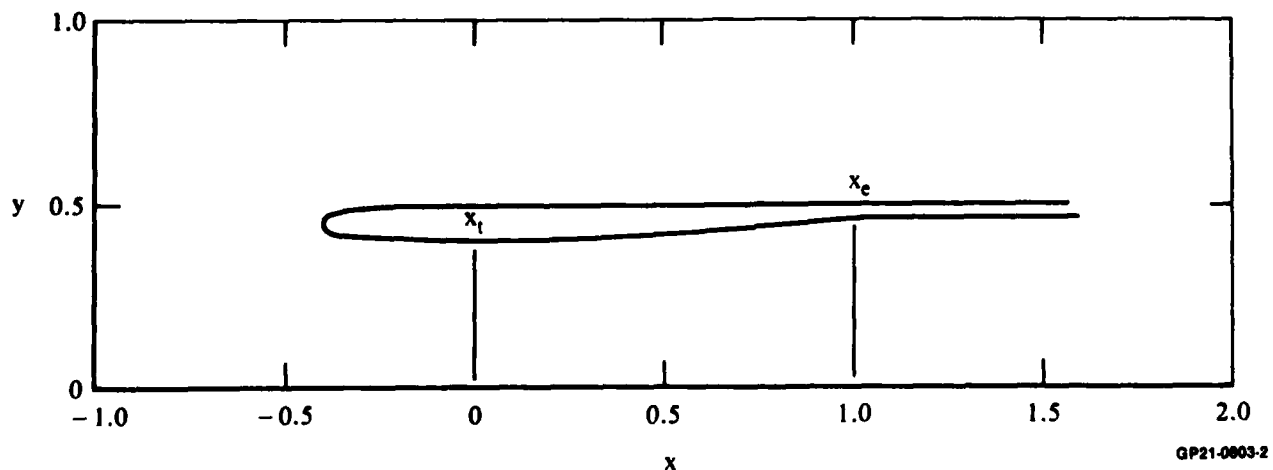


Figure 2. A converging-diverging channel.

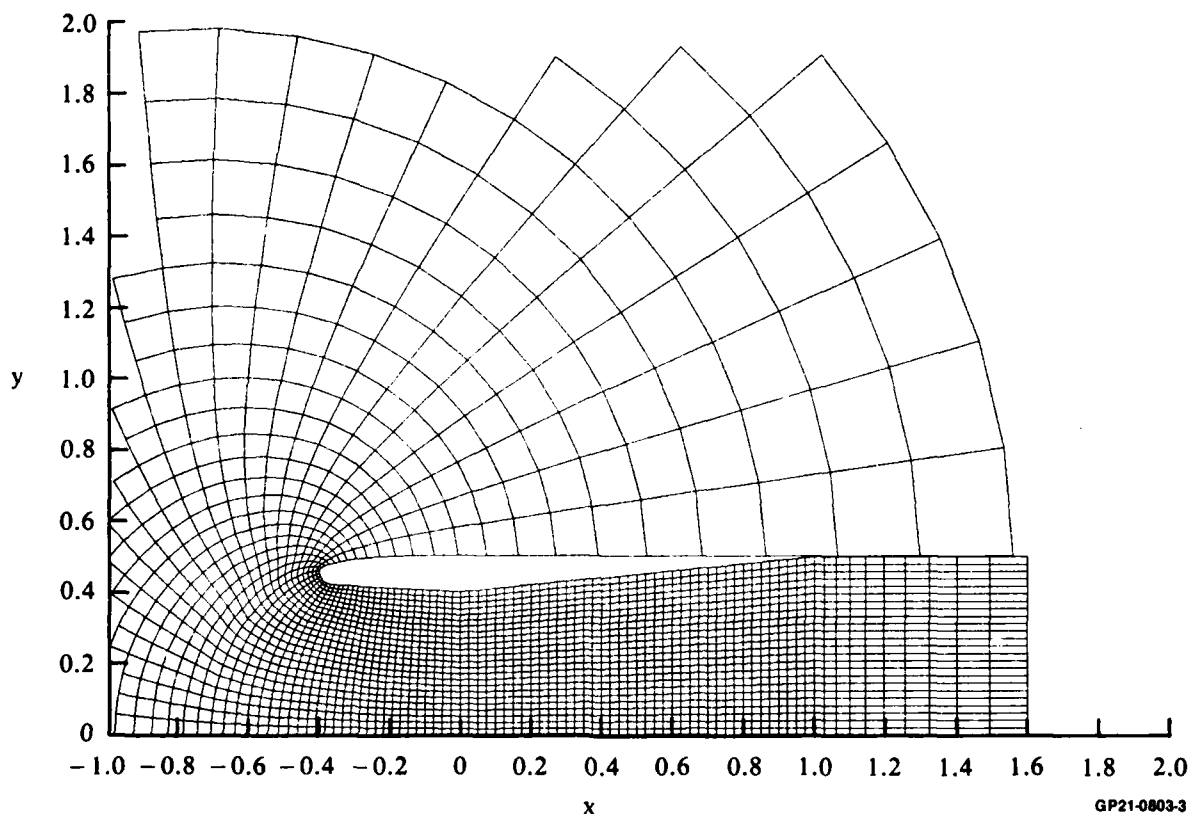


Figure 3. Grid distribution about nozzle C.

rate, the potential function at the downstream outlet boundary was frozen after 300 iterations, while the procedure continued to a total of 600 iterations. The number of supersonic points usually ceases to change in the last 50 to 200 iterations. Solutions were obtained for various slopes of the diverging wall and various inlet and exit conditions. After each flowfield computation, the total mass flux across each cross-section was computed by numerical integration:

$$\dot{m} = \int \rho u \, dy$$

or

$$\frac{\dot{m}}{\rho^* a^*} = \int_{\text{axis}}^{\text{wall}} M_X \left( 1 + \frac{\gamma-1}{2} M^2 \right)^{-3} dy, \quad (68)$$

where  $M_x$  is the component of the Mach number parallel to the nozzle axis. The nozzle flow differs from an external flow with a shock in that the flow downstream of the shock in the channel can be regarded as a potential flow with  $\rho^* = \rho_2^* = \text{constant}$ , since the variation in shock strength across the channel is relatively small. For each flowfield computation, the mass flow rate and  $a^*$  were assumed constant, and the change of the integral upstream and downstream of the shock was interpreted as a change in  $\rho^*$  across the shock.

Table 1 presents a summary of results. Channels A, B, C, D, E, and F have values of diverging wall slopes of 0.15, 0.20, 0.25, 0.40, 0.50, and

TABLE 1. SUMMARY OF CHANNEL FLOW CALCULATIONS

Case	H	Channel	$p_m$	$x_s$	$M_1$	$M_2$	$M_{2RH}$	$M_{exit}$	$\rho_2^*/\rho_1^*)_c$	$\rho_2^*/\rho_1^*)_{RH}$	$\epsilon$ (%)
1	2	A	-0.6	0.475	1.312	0.709	0.780	0.617	1.014	0.977	3.7
2	2	A	-0.3	0.475	1.312	0.713	0.780	0.621	1.011	0.977	3.4
3	2	A	0	0.475	1.312	0.713	0.780	0.620	1.011	0.977	3.4
4	2	A	0.6	0.475	1.312	0.760	0.780	0.651	0.383	0.977	0.6
5	2	A	0	0.900	1.435	0.626	0.725	0.612	1.022	0.946	7.6
6	2	C	0	0.725	1.508	0.577	0.699	0.530	1.025	0.927	9.8
7	2	D	0	0.600	1.587	0.515	0.672	0.435	1.059	0.900	15.9
8	2	D	0	1.000	1.763	0.464	0.625	0.464	1.007	0.829	17.8
9	2	B	0.6	0.150	1.200	0.792	0.843	0.580	0.992	0.993	-0.1
10	3	A	0.8	0.450	1.303	0.766	0.785	0.650	0.977	0.979	-0.2
11	3	B	0.8	0.475	1.364	0.737	0.755	0.615	0.971	0.967	0.4
12	3	B	0.8	0.575	1.402	0.788	0.739	0.665	0.930	0.958	-2.8
13	2	D	0.8	0.375	1.460	0.716	0.716	0.511	0.936	0.942	-0.6
14	2	C	0.7	0.875	1.560	0.712	0.681	0.675	0.888	0.910	-2.2
15	3	D	0.8	0.575	1.574	0.704	0.676	0.559	0.885	0.904	-1.9
16	2	E	0.8	0.725	1.726	0.656	0.634	0.558	0.826	0.845	-1.9
17	2	E	0.8	0.950	1.832	0.623	0.609	0.606	0.782	0.798	-1.6
18	2	F	0.8	0.725	1.961	0.545	0.584	0.450	0.768	0.739	2.9
19	2	F	0.8	0.975	2.110	0.568	0.560	0.558	0.660	0.670	-1.0
20	2	A	RH	0.550	1.336	0.743	0.768	0.653	0.982	0.973	0.9
21	3	B	RH	0.550	1.393	0.707	0.742	0.610	0.975	0.960	1.5
22	2	B	RH	0.550	1.393	0.708	0.742	0.610	0.973	0.960	1.3
23	3	B	RH	0.725	1.454	0.691	0.718	0.632	0.953	0.944	0.9
24	2	C	RH	0.675	1.490	0.662	0.704	0.589	0.954	0.932	2.2
25	3	D	RH	0.475	1.527	0.635	0.692	0.496	0.945	0.921	2.4
26	2	C	RH	1.000	1.602	0.655	0.668	0.657	0.896	0.894	0.2
27	2	D	RH	0.875	1.719	0.608	0.636	0.577	0.856	0.848	0.8

GP21-0803-1

0.875, respectively,  $H$  represents the order of artificial viscosity,  $p_m$  is the parameter, first introduced in Equation (55), controlling the degree of non-conservative differencing, RH in the  $p_m$  column means that the shock-point operators defined in Equations (64) or (65) were used, and  $x_s$  is the shock location.  $M_{exit}$  is the average Mach number at the channel exit;  $x_e = 1.495$  for all cases considered here.  $M_1$  and  $M_2$  are the average Mach numbers upstream and downstream of the shock. By assuming  $M = 1$  at the throat ( $x = 1$ ), the channel area ratio can be used to find a one-dimensional value of  $M_1$  at the shock. Similarly, the area ratio between  $x = x_s$  and  $x = x_e$  and  $M_{exit}$  can be used to determine a corresponding value of  $M_2$ .  $M_2)_{RH}$  is the Mach number downstream of the shock, given by the Rankine-Hugoniot relation.  $(\rho_2^*/\rho_1^*)_C$  is the stagnation density ratio across the shock, computed by numerically integrating the function given in Equation (68).  $(\rho_2^*/\rho_1^*)_{RH}$  is the analytical stagnation density ratio across a Rankine-Hugoniot shock given by Equation (63), and  $\epsilon$  is the relative error of  $(\rho_2^*/\rho_1^*)_C$  to  $(\rho_2^*/\rho_1^*)_{RH}$ . As  $p_m$  increases from 0 to 0.8,  $(\rho_2^*/\rho_1^*)_C$  decreases from near unity to a value less than  $(\rho_2^*/\rho_1^*)_{RH}$ . Smaller values of  $\epsilon$  generally mean better agreement between  $M_2$  and  $M_2)_{RH}$ .

Figure 4 compares computed shock Mach numbers,  $M_1$  and  $M_2$ , with Rankine-Hugoniot shocks and Mach numbers obtained from isentropic, mass-conserving relations. Solutions obtained by setting  $p_m = 0$  always lie below the isentropic, mass-conserving shock curve. Solutions obtained by setting  $p_m = 0.6$  to 0.8 give reasonable agreement with the Rankine-Hugoniot curve over a wide range of  $M_1$ . Solutions obtained by applying Equation (64) or (65) depend on the determination of  $M_1^*$  in Equation (63). However, in the solution process,  $M_1^*$  is chosen to be the largest value of  $M^*$  at the last two supersonic points upstream of the shock. The value of  $M_1^*$  so chosen is always smaller than the exact  $M_1^*$ ; because of the smearing of the shock over a few mesh spacings, therefore,  $M_2^*$  is in general, overpredicted. In case 26, the shock occurred at the end of the diverging section, and the prediction of  $M_1^*$  agrees with the Rankine-Hugoniot value almost exactly; flowfield gradients upstream of the shock were small, resulting in a more accurate value of  $M_2^*$ . The scatter in the computed solutions is believed to depend on the variation of Mach number across the channel, the two-dimensionality of the channel flow, and the effect of mesh spacing relative to the shock orientation.

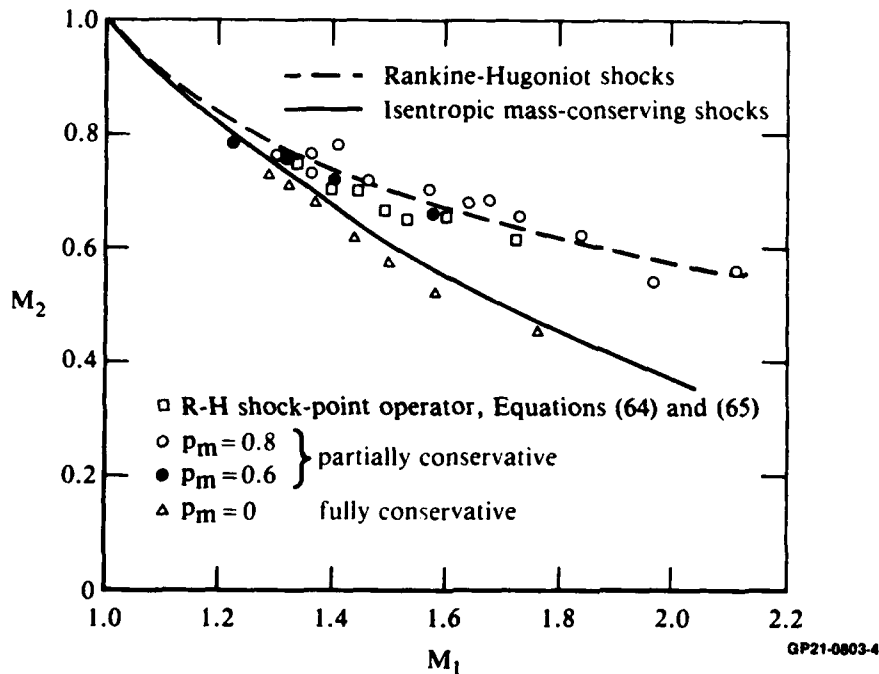


Figure 4. Comparison of computed average shock Mach number with analytical solutions.

Figure 5 presents computed values of  $\rho_2^*/\rho_1^*$  compared with the exact Rankine-Hugoniot solution. The exact solution for  $\rho_2^*/\rho_1^*$  for an isentropic, mass-conserving shock is unity. Solutions obtained with  $p_m = 0$  are all slightly greater than unity. Figures 4 and 5 are actually alternate methods of presenting the same information because of the unique relation between  $M_2^*$  and  $\rho_2^*/\rho_1^*$  for a particular value of  $M_1^*$ . Figures 6-14 present tables and line-printer plots of computed Mach number distributions on the wall and along the axis of symmetry, and Rankine-Hugoniot Mach number distributions for various cases. The columns labeled MACH-RH present the analytical one-dimensional Mach number distribution; columns labeled MACH-AXIS and MACH-WALL are computed Mach numbers distributions along the axis of symmetry and along the wall, respectively.

The preceding channel-flow calculations demonstrate that, in this instance, it is possible to obtain solutions from a potential formulation that closely approximate solutions to the Euler equations. In the flow about an airfoil or wing, the shock strength is maximum near the surface and decreases to zero with increasing distance normal to the surface. Vorticity, which is

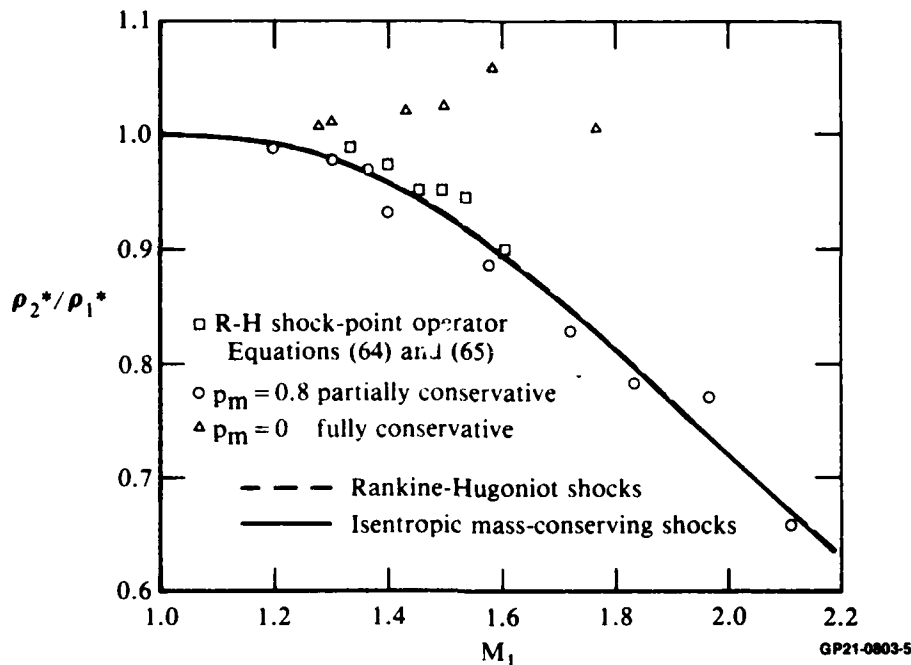
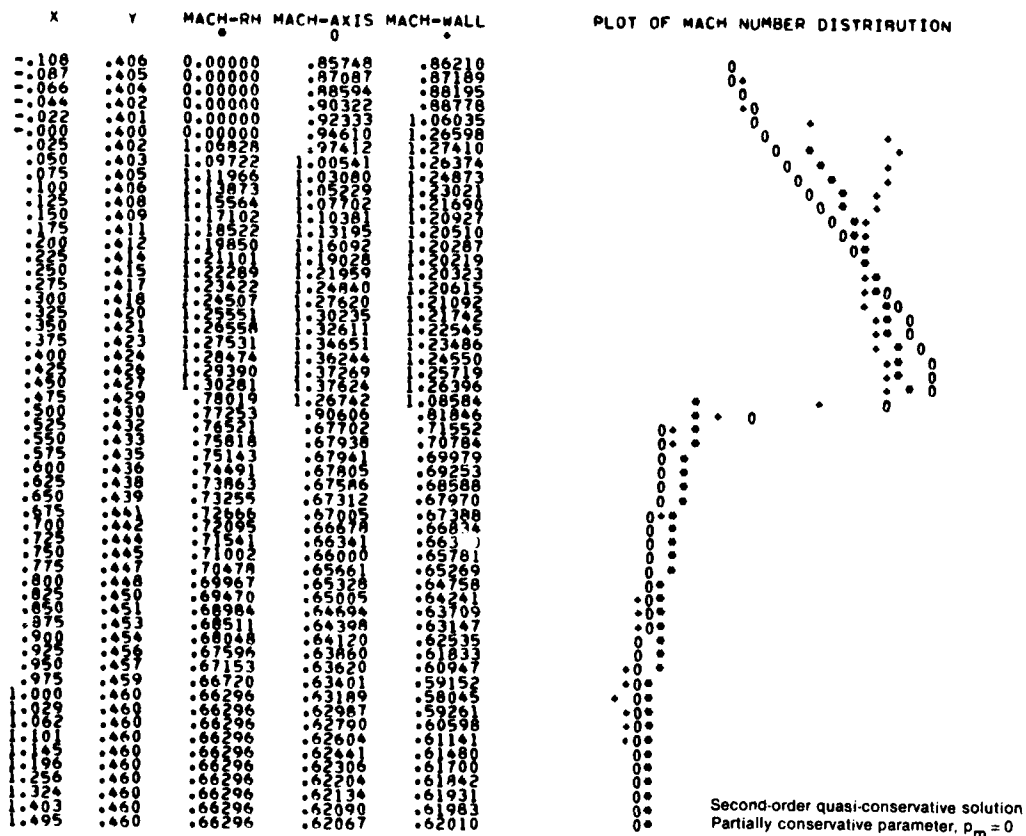
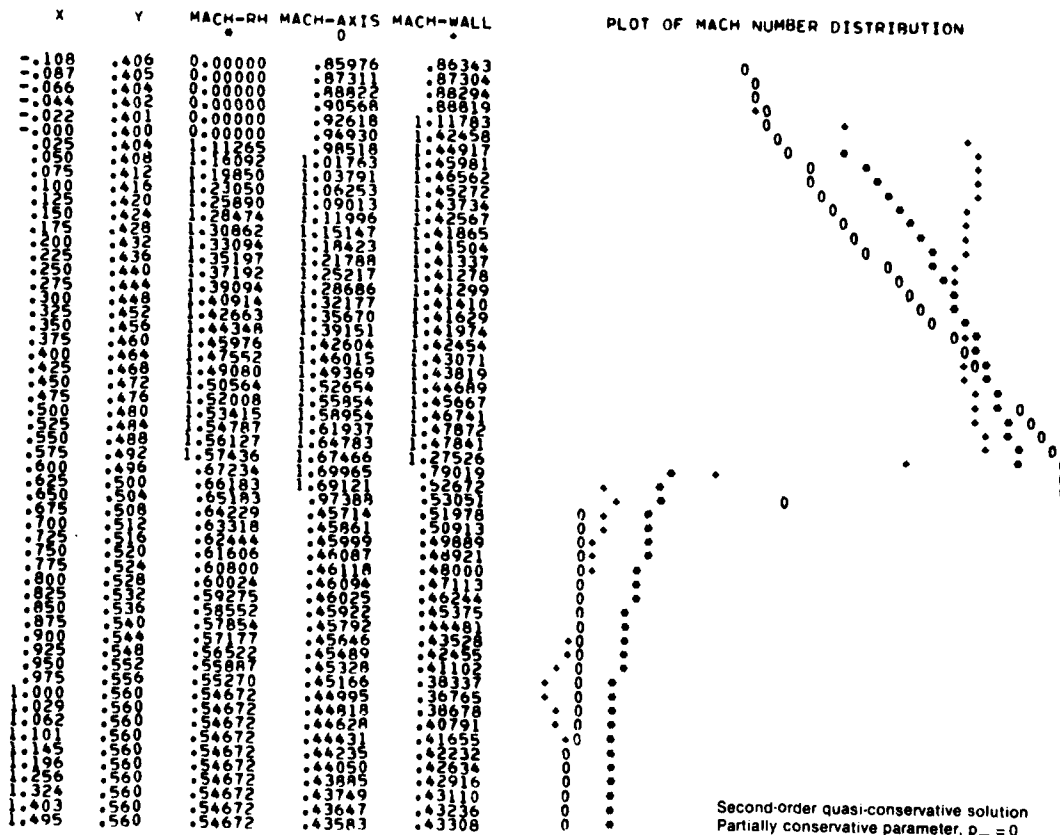


Figure 5. Comparison of computed stagnation density changes across shocks with analytical solutions.

neglected in the potential formulation, is thereby introduced into the real flow. Although the vorticity effect in transonic flowfields is of second-order,<sup>19</sup> potential flows with variable-strength shocks contain errors which can be minimized, from an engineering standpoint, but not eliminated. A good example of this is shown by Lock<sup>20</sup> who applied a partially conservative shock-point operator to compute airfoil flows. In the nonlifting case, his partially conservative solutions agree reasonably well with Euler's solutions, while in the lifting case, a discrepancy persists. Since the present work gives a shock-capturing technique resulting in Mach number jumps that are close to the Rankine-Hugoniot values, it is possible to interpret the computed velocity potential distribution downstream of the shock using the Rankine-Hugoniot values of stagnation pressure or density at each streamline, rather than with the conventional isentropic assumption. This interpretation would have the effect of carrying the inherent error in the solution from the immediate vicinity of the shock wave, where mass and momentum are now conserved, to the region downstream of the shock. Comparisons of potential flowfield computations with numerical solutions of the Euler equations are needed to evaluate the usefulness of this interpretation since comparisons involving experimental data are usually complicated by wind-tunnel wall effects and viscous-inviscid interactions.







GP21-0803-7

Figure 7. Mach number distribution of channel flow for case 7.

X	Y	MACH-RH	MACH-AXIS	MACH-WALL
.108	.406	0.00000	.85496	.85981
.087	.405	0.00000	.86772	.86944
.066	.404	0.00000	.88183	.88226
.044	.402	0.00000	.89751	.88461
.022	.401	0.00000	.91472	.86311
.000	.400	0.00000	.94068	.27533
.000	.402	.08724	.99080	.29563
.000	.404	.11869	.05840	.30511
.000	.406	.14378	.06404	.29352
.000	.408	.16537	.07571	.27233
.000	.410	.18463	.09381	.26106
.000	.412	.20162	.11781	.26289
.000	.414	.21652	.14623	.26946
.000	.416	.22937	.17771	.27326
.000	.418	.24020	.21098	.27293
.000	.420	.24990	.24511	.27048
.000	.422	.25749	.27941	.26783
.000	.424	.26292	.31340	.26589
.000	.426	.26630	.34689	.26418
.000	.428	.26767	.37887	.26240
.000	.430	.26700	.40939	.26154
.000	.432	.26532	.43744	.26039
.000	.434	.26264	.46172	.25950
.000	.436	.25902	.48012	.25888
.000	.438	.25449	.49236	.25800
.000	.440	.24907	.49813	.25683
.000	.442	.24287	.49615	.25540
.000	.444	.23600	.48679	.25382
.000	.446	.22875	.46979	.25209
.000	.448	.22123	.44584	.25036
.000	.450	.21354	.41507	.24861
.000	.452	.20579	.37844	.24684
.000	.454	.19799	.33630	.24506
.000	.456	.18921	.28944	.24328
.000	.458	.17954	.23838	.24149
.000	.460	.16920	.18291	.23970
.000	.462	.15830	.12416	.23791
.000	.464	.14697	.06332	.23612
.000	.466	.13532	.00052	.23433
.000	.468	.12346	.00000	.23254
.000	.470	.11149	.00000	.23075
.000	.472	.09942	.00000	.22896
.000	.474	.08725	.00000	.22717
.000	.476	.07498	.00000	.22538
.000	.478	.06261	.00000	.22359
.000	.480	.05014	.00000	.22180
.000	.482	.03767	.00000	.22001
.000	.484	.02520	.00000	.21822
.000	.486	.01273	.00000	.21643
.000	.488	.00026	.00000	.21464
.000	.490	.00000	.00000	.21285
.000	.492	.00000	.00000	.21106
.000	.494	.00000	.00000	.20927
.000	.496	.00000	.00000	.20748
.000	.498	.00000	.00000	.20569
.000	.500	.00000	.00000	.20390
.000	.502	.00000	.00000	.20211
.000	.504	.00000	.00000	.20032
.000	.506	.00000	.00000	.19853
.000	.508	.00000	.00000	.19674
.000	.510	.00000	.00000	.19495
.000	.512	.00000	.00000	.19316
.000	.514	.00000	.00000	.19137
.000	.516	.00000	.00000	.18958
.000	.518	.00000	.00000	.18779
.000	.520	.00000	.00000	.18600
.000	.522	.00000	.00000	.18421
.000	.524	.00000	.00000	.18242
.000	.526	.00000	.00000	.18063
.000	.528	.00000	.00000	.17884
.000	.530	.00000	.00000	.17705
.000	.532	.00000	.00000	.17526
.000	.534	.00000	.00000	.17347
.000	.536	.00000	.00000	.17168
.000	.538	.00000	.00000	.16989
.000	.540	.00000	.00000	.16810
.000	.542	.00000	.00000	.16631
.000	.544	.00000	.00000	.16452
.000	.546	.00000	.00000	.16273
.000	.548	.00000	.00000	.16094
.000	.550	.00000	.00000	.15915
.000	.552	.00000	.00000	.15736
.000	.554	.00000	.00000	.15557
.000	.556	.00000	.00000	.15378
.000	.558	.00000	.00000	.15199
.000	.560	.00000	.00000	.15020
.000	.562	.00000	.00000	.14841
.000	.564	.00000	.00000	.14662
.000	.566	.00000	.00000	.14483
.000	.568	.00000	.00000	.14304
.000	.570	.00000	.00000	.14125
.000	.572	.00000	.00000	.13946
.000	.574	.00000	.00000	.13767
.000	.576	.00000	.00000	.13588
.000	.578	.00000	.00000	.13409
.000	.580	.00000	.00000	.13230
.000	.582	.00000	.00000	.13051
.000	.584	.00000	.00000	.12872
.000	.586	.00000	.00000	.12693
.000	.588	.00000	.00000	.12514
.000	.590	.00000	.00000	.12335
.000	.592	.00000	.00000	.12156
.000	.594	.00000	.00000	.11977
.000	.596	.00000	.00000	.11798
.000	.598	.00000	.00000	.11619
.000	.600	.00000	.00000	.11440
.000	.602	.00000	.00000	.11261
.000	.604	.00000	.00000	.11082
.000	.606	.00000	.00000	.10903
.000	.608	.00000	.00000	.10724
.000	.610	.00000	.00000	.10545
.000	.612	.00000	.00000	.10366
.000	.614	.00000	.00000	.10187
.000	.616	.00000	.00000	.10008
.000	.618	.00000	.00000	.09829
.000	.620	.00000	.00000	.09650
.000	.622	.00000	.00000	.09471
.000	.624	.00000	.00000	.09292
.000	.626	.00000	.00000	.09113
.000	.628	.00000	.00000	.08934
.000	.630	.00000	.00000	.08755
.000	.632	.00000	.00000	.08576
.000	.634	.00000	.00000	.08397
.000	.636	.00000	.00000	.08218
.000	.638	.00000	.00000	.08039
.000	.640	.00000	.00000	.07860
.000	.642	.00000	.00000	.07681
.000	.644	.00000	.00000	.07502
.000	.646	.00000	.00000	.07323
.000	.648	.00000	.00000	.07144
.000	.650	.00000	.00000	.06965
.000	.652	.00000	.00000	.06786
.000	.654	.00000	.00000	.06607
.000	.656	.00000	.00000	.06428
.000	.658	.00000	.00000	.06249
.000	.660	.00000	.00000	.06070
.000	.662	.00000	.00000	.05891
.000	.664	.00000	.00000	.05712
.000	.666	.00000	.00000	.05533
.000	.668	.00000	.00000	.05354
.000	.670	.00000	.00000	.05175
.000	.672	.00000	.00000	.04996
.000	.674	.00000	.00000	.04817
.000	.676	.00000	.00000	.04638
.000	.678	.00000	.00000	.04459
.000	.680	.00000	.00000	.04280
.000	.682	.00000	.00000	.04101
.000	.684	.00000	.00000	.03922
.000	.686	.00000	.00000	.03743
.000	.688	.00000	.00000	.03564
.000	.690	.00000	.00000	.03385
.000	.692	.00000	.00000	.03206
.000	.694	.00000	.00000	.03027
.000	.696	.00000	.00000	.02848
.000	.698	.00000	.00000	.02669
.000	.700	.00000	.00000	.02490
.000	.702	.00000	.00000	.02311
.000	.704	.00000	.00000	.02132
.000	.706	.00000	.00000	.01953
.000	.708	.00000	.00000	.01774
.000	.710	.00000	.00000	.01595
.000	.712	.00000	.00000	.01416
.000	.714	.00000	.00000	.01237
.000	.716	.00000	.00000	.01058
.000	.718	.00000	.00000	.00879
.000	.720	.00000	.00000	.00700
.000	.722	.00000	.00000	.00521
.000	.724	.00000	.00000	.00342
.000	.726	.00000	.00000	.00163
.000	.728	.00000	.00000	.00000

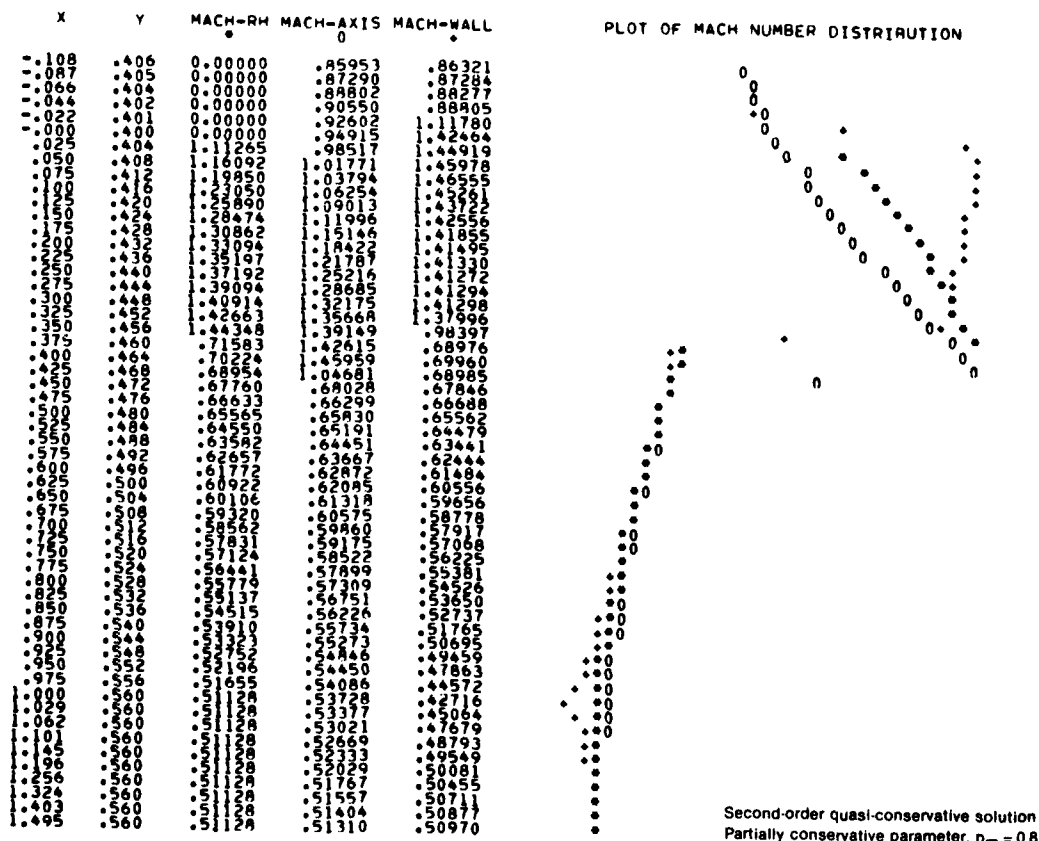
PLOT OF MACH NUMBER DISTRIBUTION



Third-order quasi-conservative solution  
Partially conservative parameter,  $\rho_m = 0.8$

GP21-0803-8

Figure 8. Mach number distribution of channel flow for case 12.



GP21-0803-9

Figure 9. Mach number distribution of channel flow for case 13.

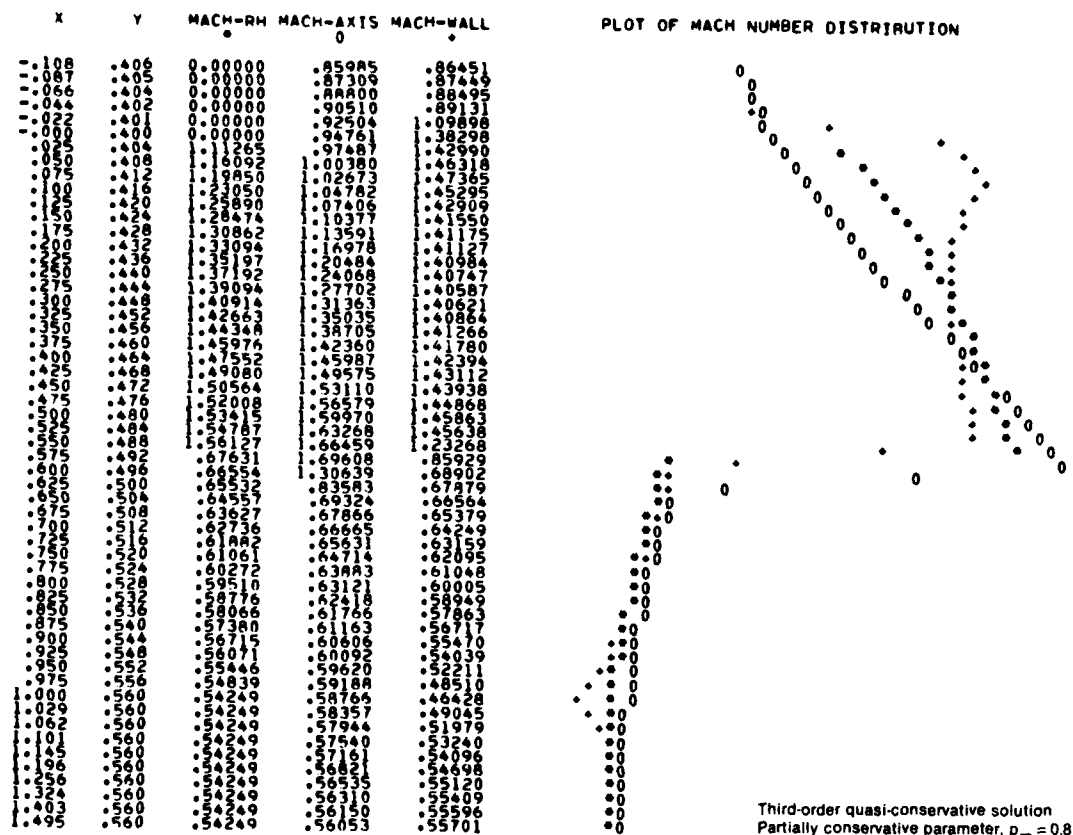
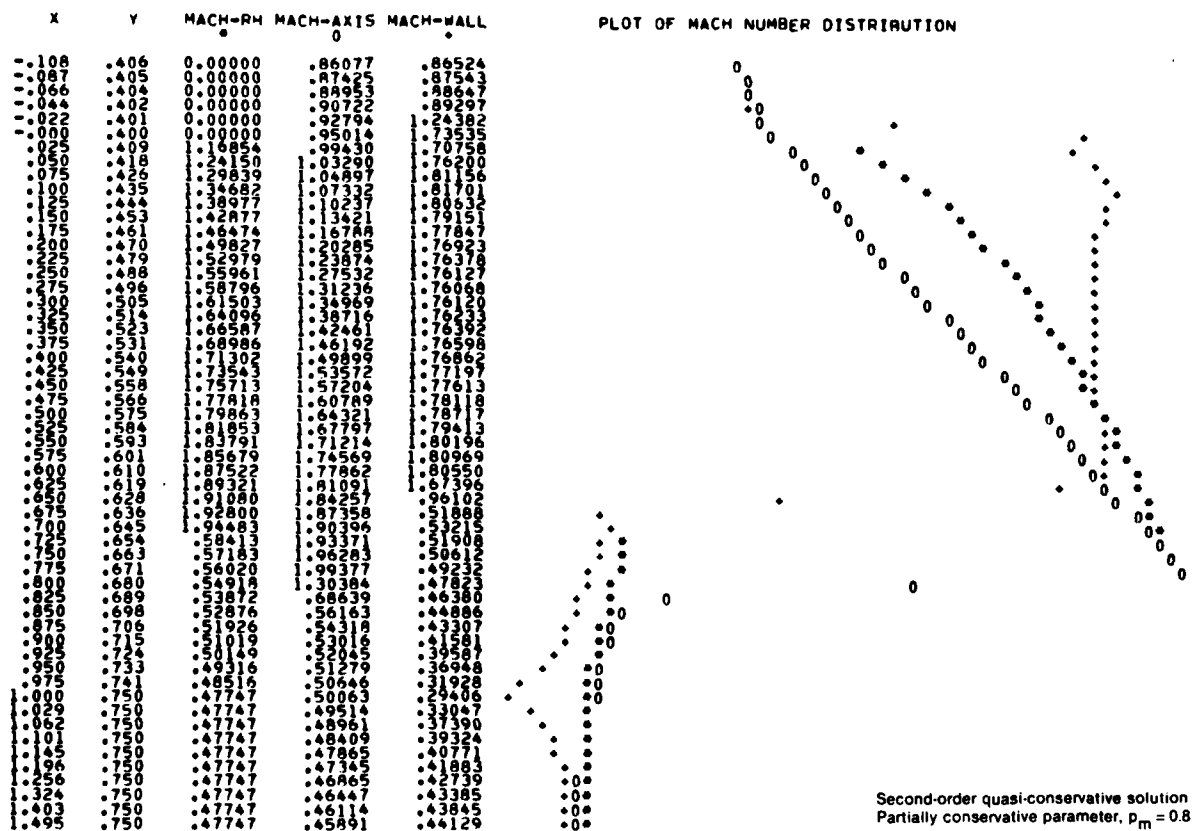
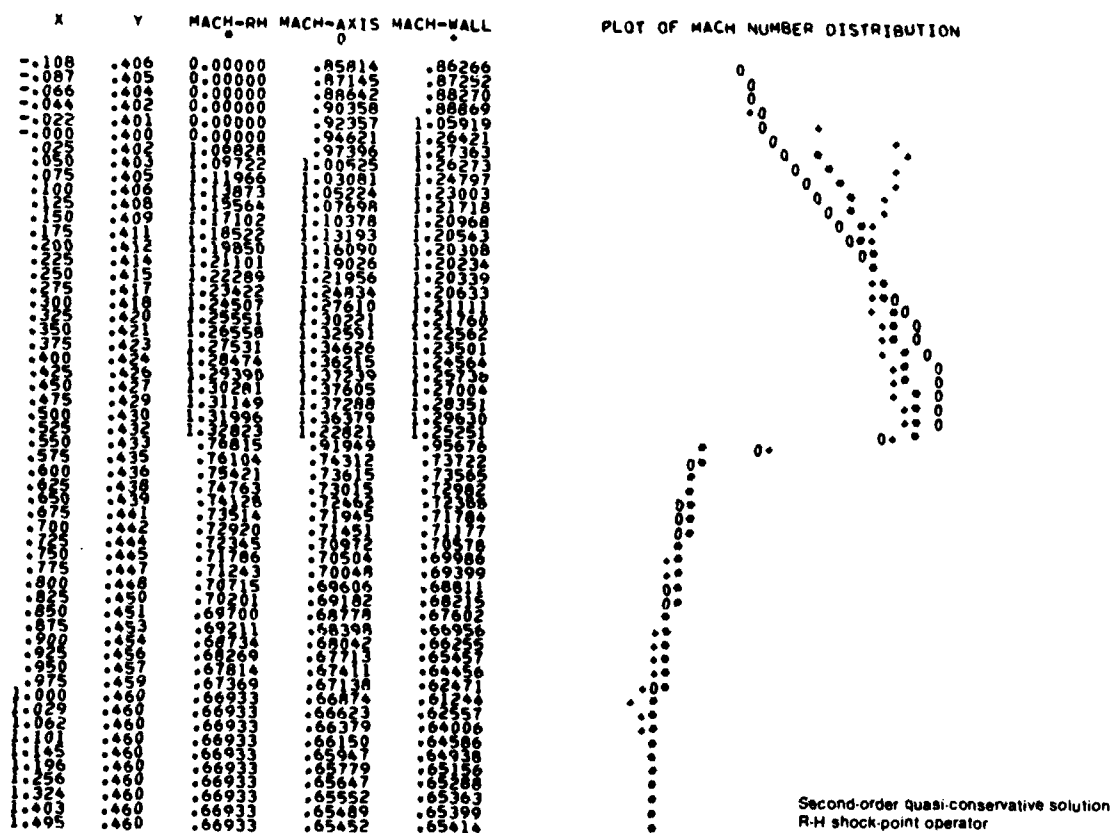


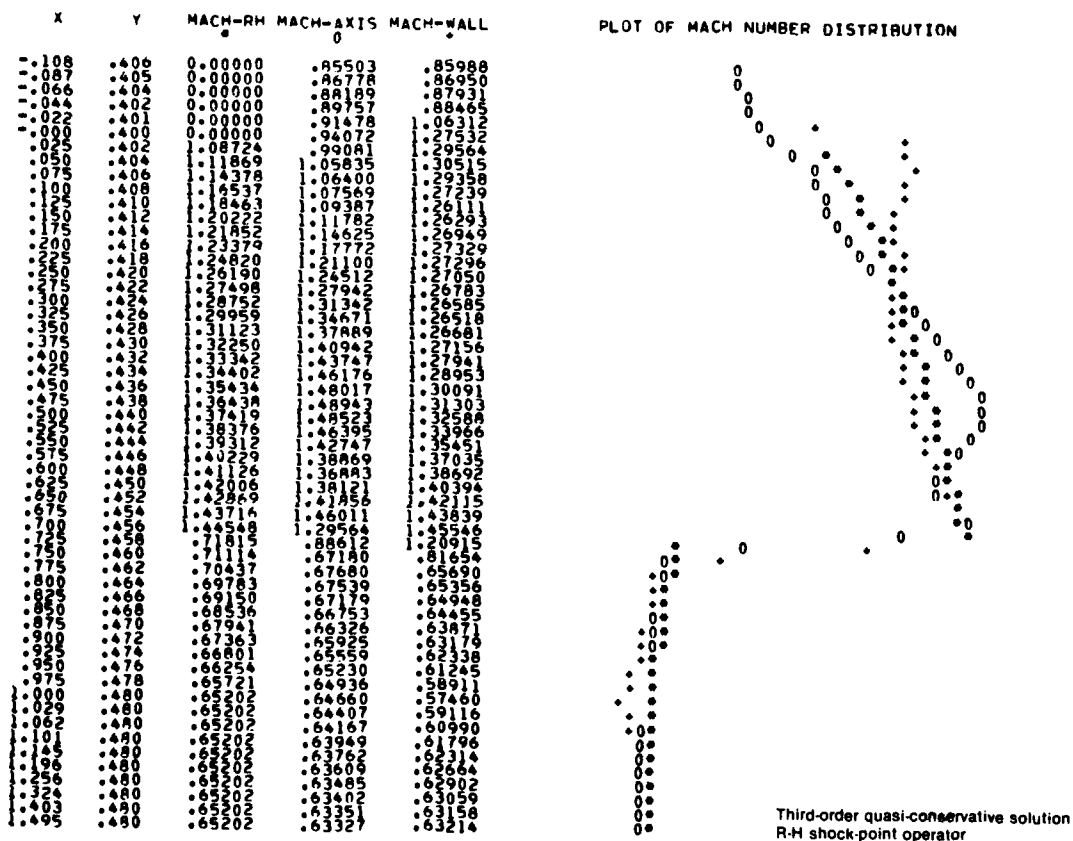
Figure 10. Mach number distribution of channel flow for case 15.



GP21-0803-11

Figure 11. Mach number distribution of channel flow for case 18.





GP21-0803-13

Figure 13. Mach number distribution of channel flow for case 23.





## 6. WING-BODY FLOWFIELD COMPUTATIONS

### 6.1 Grid Generation and Computational Domain

The finite-difference approximation of the governing equation obtained in the previous section can be constructed with the knowledge of mesh-point locations. The coordinate transformation derivatives are found at each control point within a local second-order element shown in Figure 1. Any scheme that generates a grid system in a regular computational domain can be incorporated with the finite-difference equation solver.

In the present study, a grid-generation scheme developed in Reference 21 is applied. The transformation of the physical space to the computational space is shown in Figure 15. The computational space is truncated at a finite distance from the wing surface. For the results presented here, the far-field boundary is placed approximately five to six root-chord lengths from the wing surface in the streamwise and surface normal directions, and the spanwise far field is located two to three semi-span lengths from the wing tip and the outboard far-field. C-type meshes are generated which wrap around the fuselage nose and wing leading edge. Outboard of the wing tip, the mesh wraps around a surface extending from the wing tip to the outboard farfield. Details of the grid-generation scheme can be found in Reference 21.

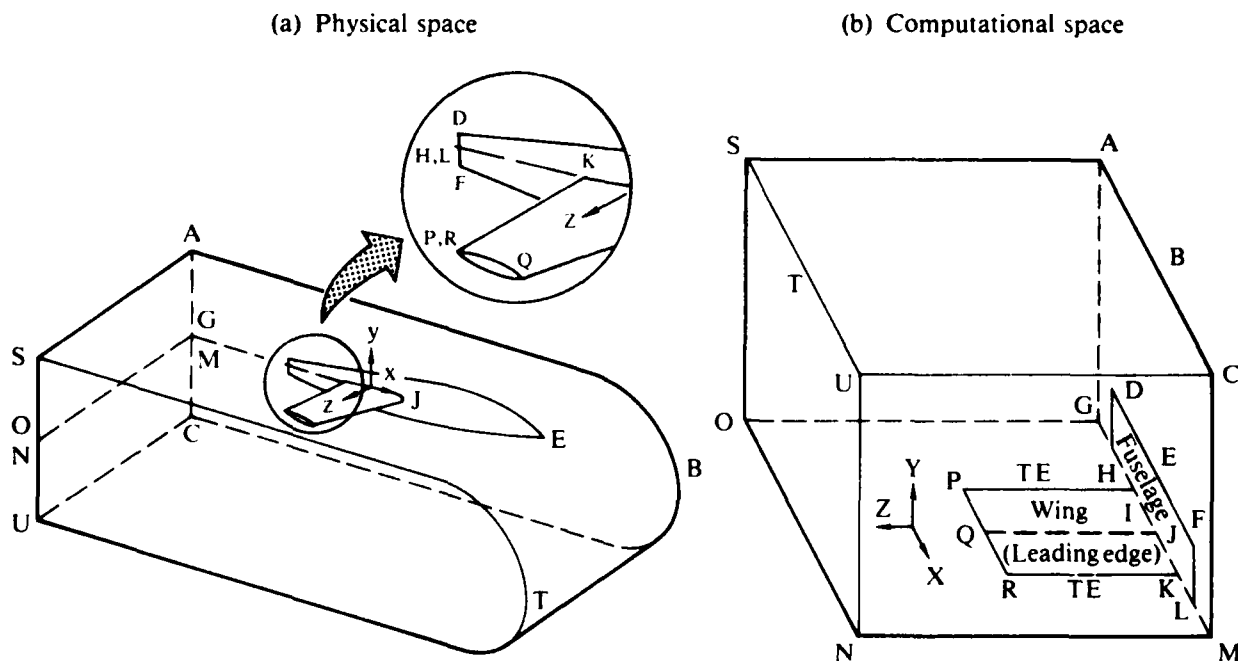


Figure 15. Physical and computational domain for a wing-fuselage configuration.

GP21-0803-16

Typical grids used in the present calculation are presented in Figures 16 and 17. Figure 16 shows the grid distribution on an ONERA-M6 wing on a vertical wall, and Figure 17 shows the grid distribution on the same wing on a semi-infinite fuselage.

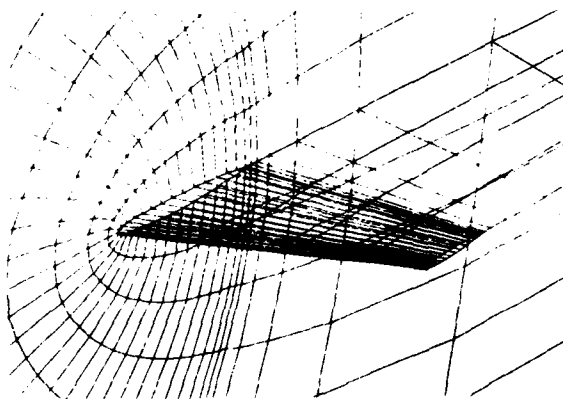
## 6.2 Boundary Conditions

The necessary boundary conditions include the impermeability condition on the wing and fuselage surfaces, the Kutta condition along the trailing edge, the zero streamwise variation on the downstream Trefftz plane, and the free-stream condition on the other farfield boundaries. For easy implementation of the far-field freestream condition, a reduced potential,  $G$ , representing a perturbation from the freestream, is introduced according to

$$\phi = U_{\infty} (x \cos \alpha + y \sin \alpha + G), \quad (69)$$

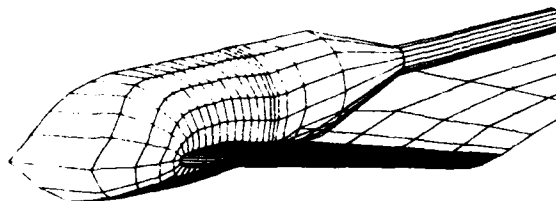
where  $U_{\infty}$  is the freestream velocity and  $\alpha$  is the angle of attack.

On the boundary cross-planes, ACUSA and SUNOS,  $G$  is set to zero, representing the freestream condition. On the Trefftz plane or the boundary cross-plane AGOSA and CMNUC, the streamwise variations are assumed to be zero; therefore, the following two-dimensional equation is applied:



QP21-0803-26

Figure 16. Grid distribution on an ONERA-M6 wing and a vertical wall.



QP21-0803-27

Figure 17. Grid distribution on an ONERA-M6 wing and a simplified fuselage.

$$c_2\phi_{YY} + c_3\phi_{ZZ} + c_5\phi_{YZ} + c_8\phi_Y + c_9\phi_Z = 0. \quad (70)$$

Equation (70) is obtained from Equation (8) by neglecting all derivatives in the X-direction.

On the fuselage and wing surfaces, the impermeability condition is applied:

$$V = 0, \text{ on the wing surface,} \quad (71)$$

and

$$W = 0, \text{ on the fuselage surface.} \quad (72)$$

Exact surface-boundary conditions can be enforced at boundary points by substituting Equations (19) and (20) into Equations (71) and (72), respectively, and solving the equations for the value of the potential function at boundary points. One-sided differencing is used in the surface-normal direction so that there is no need to extrapolate the potential to imaginary points inside the wing or fuselage surfaces. However, Equation (72) might not be suitable for highly distorted grids near the fuselage and wing intersection. Boundary conditions obtained from the finite-volume algorithm<sup>1</sup> give better results near the intersection. Therefore all solutions presented in the subsequent section were obtained by applying the finite-volume surface-boundary condition in the cross-plane ACMG.

Along the trailing edge, the linearized equation

$$(h_1^2 + h_2^2 + h_3^2)\phi_{XX} + (h_4^2 + h_5^2 + h_6^2)\phi_{YY} + (h_7^2 + h_8^2 + h_9^2)\phi_{ZZ} = 0 \quad (73)$$

is assumed to hold. Equation (73) is obtained from Equation (8) by neglecting the nonlinear velocity contribution and the cross- and first-derivative terms. This linearized equation is approximately valid along the trailing edge only for wing cross-sections having a finite trailing-edge angle where zero flow velocity can be approximately assumed; Equation (73) can be regarded as an interpolation operator when the wing trailing edge is cusped. The circulation  $\Gamma$  at each spanwise location is determined iteratively as the solution proceeds. Constant discontinuities in potential across the cut

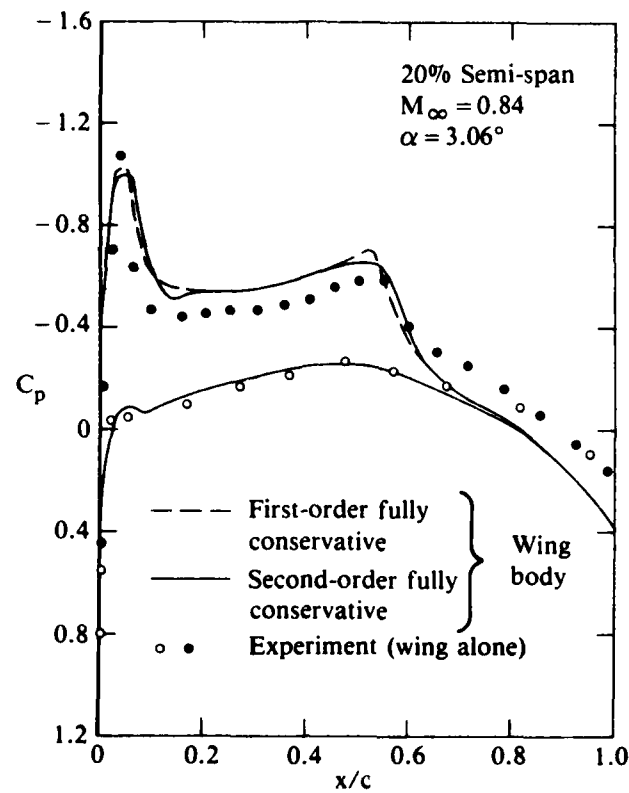
downstream of the trailing edge are enforced along the streamwise coordinate lines extending from the trailing edge to the downstream far-field. The value of the discontinuity in each spanwise plane is computed at the trailing edge by satisfying Equation (73) at both the upper and lower trailing edges.

Beyond the wing tip, the continuity of the potential function across the surface about which the mesh is unwrapped can be approximated by solving  $\phi_{yy} = 0$  at points on this surface and just next to the tip. The same condition is applied in the FLO-22 code<sup>22</sup> to solve for the potential function at points lying on the vortex sheet.

### 6.3 Numerical Results

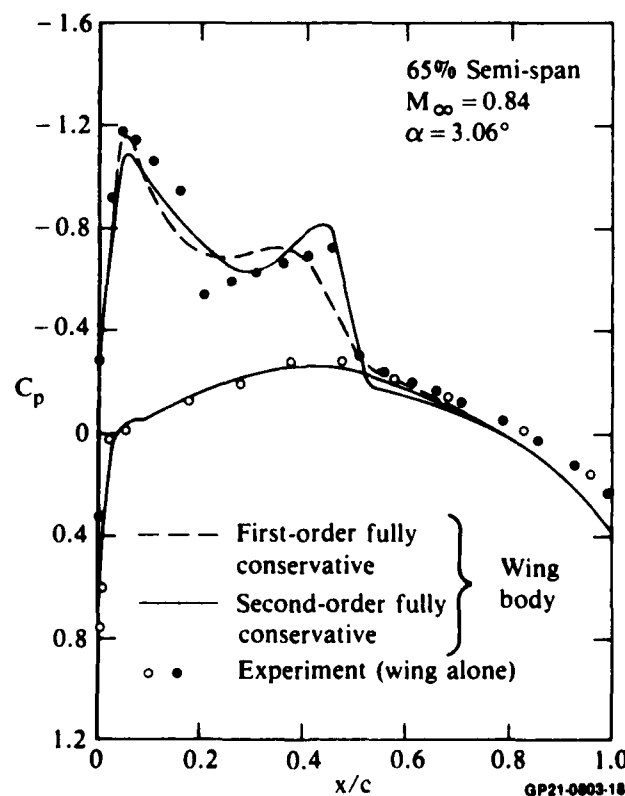
Typical solutions obtained using the second- and third-order, quasi-conservative and fully conservative schemes are presented in this section. Two meshes are used in all calculations. The coarse mesh contains 44 mesh cells in the X-direction, 10 mesh cells in the Y-direction, and 7 mesh cells in the Z-direction, where 32 x 5 mesh cells are on the unwrapped wing surface. The fine mesh has double the number of mesh cells in each direction. Two-hundred relaxation sweeps were performed on the coarse mesh, followed by two-hundred relaxation sweeps on the fine mesh.

Figures 18 and 19 present comparisons of first- and second-order fully conservative solutions obtained for the ONERA-M6 wing on a semi-infinite fuselage shown in Figure 17. The fuselage has a constant radius of 0.2 semi-span length, measured from the wing root to wing tip, in the section of the wing-fuselage intersection. There are no experimental data for this configuration; however, experimental data are available for the same wing on a vertical wall in Reference 23. Computed solutions at 20% and 65% semi-span locations are presented in Figures 18 and 19, respectively, for  $M_\infty = 0.84$  and  $\alpha = 3.06^\circ$ , where  $\alpha$  is the angle of attack and also the angle of incidence between the wing and fuselage. The fuselage effect is not pronounced in this case, and agreement between the computed solutions and experiment is generally good. At the 20% semi-span location, the first-order solution agrees with the second-order solution except for minor differences in suction peaks and details at the shocks. At the 65% semi-span location, experimental data show a distinct double shock on the upper surface. The second-order solution obviously resolves this double shock better than the first-order solution,



GP21-0803-17

Figure 18. Comparison of first- and second-order fully conservative solutions.



GP21-0803-18

Figure 19. Comparison of first- and second-order fully conservative solutions.

although there are still small discrepancies between the second-order solution and experiment, presumably because the mesh used for the computation is relatively coarse.

In Figures 20-24 pressure distributions obtained for an ONERA-M6 wing on a wall, Figure 16, are shown and compared with experimental data.<sup>23</sup> The free-stream Mach number is 0.84 and the angle of attack is  $3.06^\circ$ . Second-order quasi-conservative and first- and second-order fully conservative solutions were obtained at the 20%, 65%, and 95% semi-span locations and are shown in Figures 20-22. At the 20% semi-span location, numerical solutions predict lower suction peaks. The plateau pressures at the 20% and 65% semi-span locations are slightly overpredicted, while the pressures downstream of the shocks are slightly higher than the experimental data. The locations of shocks are predicted accurately by the numerical solutions. Although the mesh used is still relatively coarse, the overall agreement between the numerical and experimental results is satisfactory. The quasi-conservative solutions

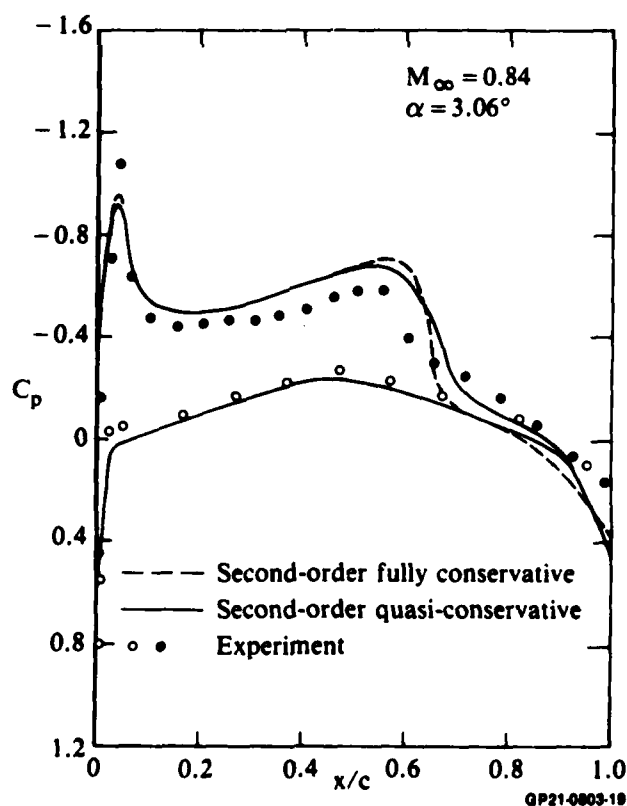


Figure 20. Pressure distributions on the upper and lower surfaces of an ONERA wing on a wall at the 20% semi-span location.

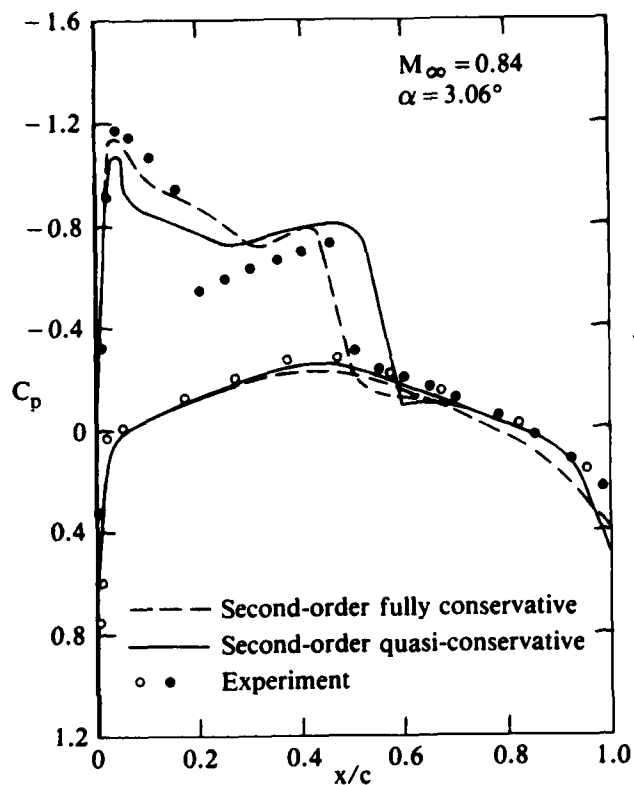


Figure 21. Pressure distributions on the upper and lower surfaces of an ONERA-M6 wing on a wall at the 65% semi-span location.

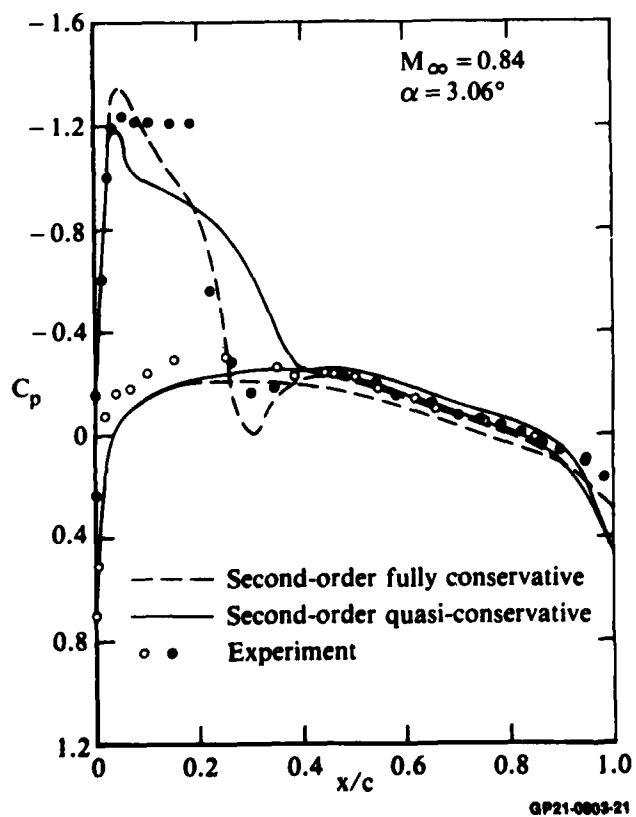


Figure 22. Pressure distribution on the upper and lower surfaces of an ONERA-M6 wing on a wall at the 95% semi-span location.

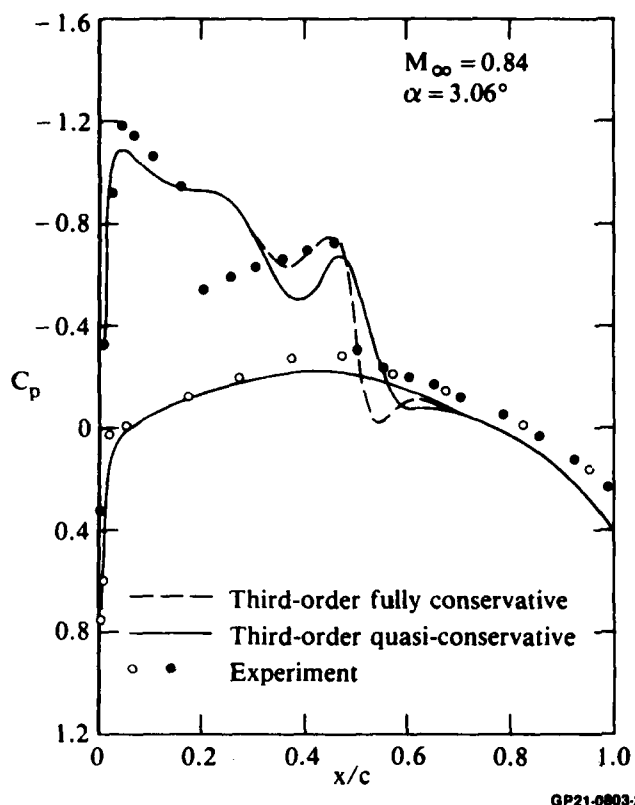


Figure 23. Comparison of third-order quasi-conservative and fully conservative solutions at the 65% semi-span location.

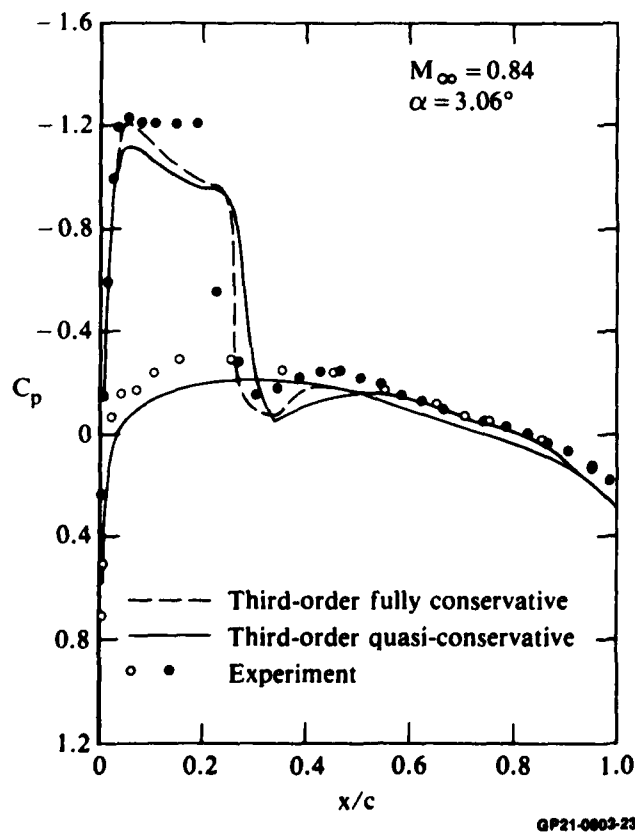


Figure 24. Comparison of third-order quasi-conservative and fully conservative solutions at the 95% semi-span location.



predict a more positive pressure at the trailing edge and yield better agreement with experimental data upstream of the trailing edge. This result is apparently attributable to enforcement of the exact surface boundary condition and the linearized equation, Equation (73), which approximately simulates a flow stagnation condition for finite trailing-edge angles, as mentioned previously. However, the quasi-conservative solutions predict a more-downstream shock location at a 65% semi-span location and do not resolve the suction peak as well as the fully conservative scheme. The poor resolution of the suction peak is caused by the second-order element not resolving the surface curvature and potential gradient near the leading edge as the exact surface-boundary condition is enforced. The leading-edge resolution can be significantly improved by using a third-order element as shown in Reference 7.

Third-order, quasi-conservative and fully conservative solutions are obtained for the same wing and compared with experiment in Figures 23 and 24 at the 65% and 95% semi-span locations, respectively. The finite-volume boundary conditions were applied on the airfoil surface for both solutions. The pressure distributions in the supersonic region are more accurately predicted at the 95% semi-span location than in the second-order solutions shown in Figure 20, although the plateau pressure still is underpredicted. A triple shock is found in the computed pressure distribution at the 65% semi-span location, although the first shock is somewhat ambiguous. This pattern also appears at spanwise locations between 50% and 70%. Evidence of the triple shock is not shown in the experimental data; however, triple-shock structures have been observed in static-pressure distributions obtained with other wings at transonic speeds. This feature probably is not associated with poor convergence since the solutions presented here have all converged to sufficiently small residuals. It is also possible that the triple-shock pattern is the result of a numerical oscillation caused by interaction between the numerical frequency of the third-order artificial viscosity and the wave frequency associated with the double shock. To explain the characteristics of the third-order solutions, finer-mesh solutions are needed.

A study of the shock-point operator for the same ONERA-M6 wing on the wall at  $M_\infty = 0.84$  and  $\alpha = 3.06$  is shown in Figures 25 and 26. As mentioned previously,  $p_m$  is the parameter controlling the nonconservative differencing of the shock-point operators in Equations (61) and (64). Solutions are

obtained for  $p_m = 0, 1, \text{ and } 2$  at 20% and 65% semi-span locations by using the second-order artificial viscosity at supersonic points. A second-order fully conservative solution is obtained as  $p_m = 0$ . As  $p_m$  increases, the amount of nonconservative differencing increases, and the additional mass flux introduced at the shock increases. By adjusting the value of  $p_m$ , part of shock-induced boundary-layer displacement effect can be simulated. By increasing the value of  $p_m$ , the shock moves upstream, the shock strength decreases, and agreement of the computed pressure with experimental data is significantly improved both upstream and downstream of the shocks. Solutions obtained by setting  $p_m = 2$  seem to yield best agreement with experiments.

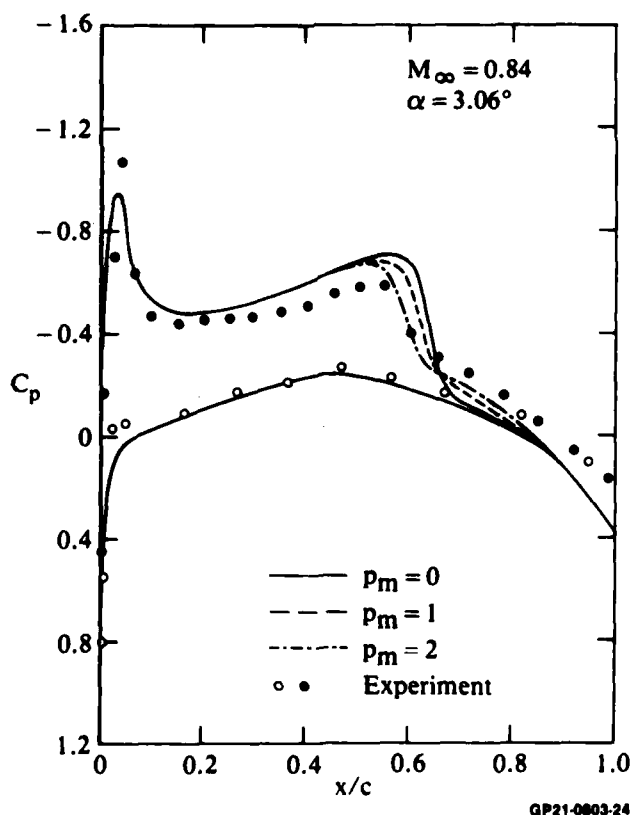
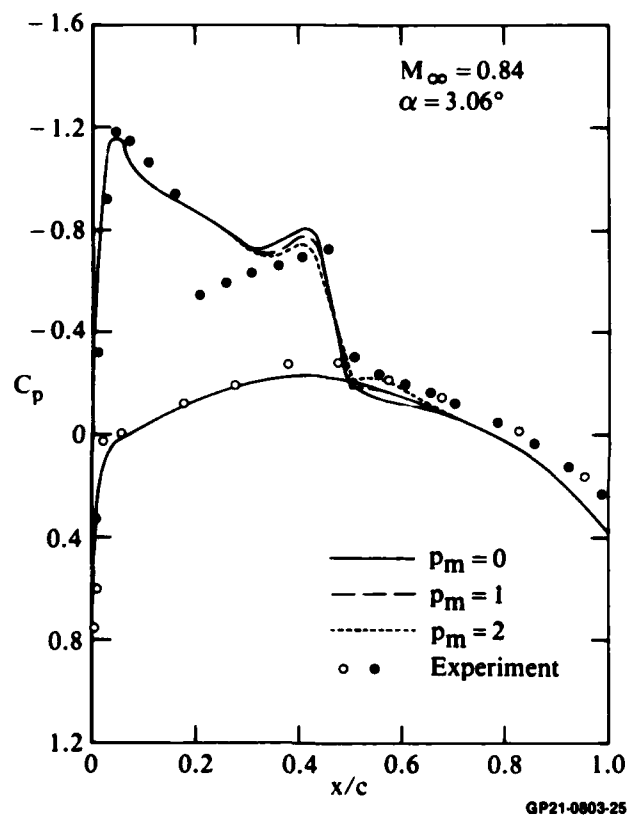


Figure 25. Study of partially conservative shock-point operators at 20% semi-span location on an ONERA-M6 wing.



**Figure 26. Study of partially conservative shock-point operators at 65% semi-span location on an ONERA-M6 wing.**

## 7. CONCLUSIONS

Second- and third-order, fully conservative and quasi-conservative schemes have been developed to compute flowfields about transonic wings and wing-body configurations. The quasi-conservative scheme was developed by solving a finite-difference representation of a transformed full potential equation formulated in this report and enforcing an exact body surface-boundary condition.

The second-order solutions obtained have been shown to provide better resolution for a double shock than the conventional first-order schemes. The third-order solutions show a triple-shock pattern. Additional study will be required to determine whether this pattern is a real flowfield characteristic or a feature of the numerical scheme. The enforcement of an exact surface-boundary condition in the quasi-conservative scheme provides solutions with better agreement with experiments upstream of the trailing edge.

A partially conservative shock-point operator is introduced to control the amount of nonconservative differencing at shock points and thus modify the location and strength of shocks. Proper choice of the shock-point operator significantly improves the agreement of computed pressure distribution with experimental data near the shocks. A new shock point operator is derived from an approximate one-dimensional flow analysis which properly considers the stagnation density change across the shock and predicts shocks in reasonable agreement with Rankine-Hugoniot shocks.

#### ACKNOWLEDGMENT

The author wishes to express his gratitude to D. A. Caughey for many helpful discussions and to F. W. Spaid and R. J. Hakkinen for their fruitful comments on the new shock point operator.

## REFERENCES

1. A. Jameson and D. A. Caughey, A Finite-Volume Method for Transonic Potential Flow Calculations, Proceedings of AIAA 3rd Computational Fluid Dynamics Conference, (AIAA, New York, 1977), pp. 35-54.
2. D. A. Caughey and A. Jameson, Progress in Finite-Volume Calculations for Wing-Fuselage Combinations, AIAA J. 18, 1281 (1980).
3. G. E. Chmielewski, Transonic Wing/Body Flow Analysis Using Non-Surface-Fitted Coordinates, AIAA Paper No. 81-0384 (1981).
4. F. R. Bailey and W. F. Ballhaus, Relaxation Methods for Transonic Flow About Wing-Cylinder Combinations and Lifting Swept Wings. Lecture Notes in Physics, (Springer-Verlag, 1972), Vol. 19.
5. C. W. Boppe, Computational Transonic Flow About Realistic Aircraft Configurations, AIAA Paper No. 78-104 (1978).
6. A. Jameson, Transonic Potential Flow Calculations Using Conservative Form, Proceedings of AIAA 2nd Computational Fluid Dynamics Conference, (AIAA, New York, 1975), pp. 148-161.
7. L. T. Chen, Improved Finite-Difference Scheme for Transonic Airfoil Flowfield Calculations, AIAA J. 20, 218 (1982).
8. D. C. Ives and J. F. Liutermoza, Second-Order-Accurate Calculation of Transonic Flow Over Turbomachinery Cascades, AIAA J. 17, 870 (1979).
9. D. A. Caughey and A. Jameson, Basic Advances in the Finite Volume Method for Transonic Potential Flow Calculations, Proceedings of Symposium on Numerical and Physical Aspects of Aerodynamic Flows, T. Cebeci, ed. (Springer-Verlag, in press).

10. A. Jameson, Acceleration of Transonic Potential Flow Calculations on Arbitrary Meshes by the Multiple Grid Methods, Proceedings of AIAA 4th Computational Fluid Dynamics Conference, (AIAA, New York, 1979), pp. 122-146.
11. L. T. Chen and D. A. Caughey, On Various Treatments of Potential Equations at Shocks, Symposium on Numerical Boundary Condition Procedures and Multi-Grid Methods, NASA Ames Research Center, Moffett Field, CA, 19-22 Oct 1981.
12. E. M. Murman, Analysis of Embedded Shock Waves Calculated by Relaxation Method, AIAA J. 12, 616 (1974).
13. M. M. Hafez and H. K. Cheng, Shock-Fitting Applied to Relaxation Solutions of Transonic Small Disturbance Equations, AIAA J. 15, 786 (1977).
14. A. Jameson, Transonic Potential Flow Calculations Using Conservative Form, Proceedings of AIAA 2nd Computational Fluid Dynamics Conference, (AIAA, New York, 1975), pp. 148-161.
15. L. T. Chen and D. A. Caughey, Calculation of Transonic Inlet Flowfields Using Generalized Coordinates, J. Aircraft 17, 167 (1980).
16. L. T. Chen and D. A. Caughey, Higher-Order Finite-Difference Scheme for Three-Dimensional Transonic Flowfields About Axisymmetric Bodies, J. Aircraft 17, 668 (1980).
17. F. T. Lynch, Recent Applications of Advanced Computational Methods in the Aerodynamic Design of Transport Aircraft Configurations, Douglas Paper No. 6639, 11th Congress of ICAS, Lisbon, Portugal, 1978.
18. A. Jameson, Iterative Solution of Transonic Flows Over Airfoils and Wings, Including Flows at Mach 1, Comm. Pure Appl. Math. 27, 283 (1974).
19. W. D. Hayes, La seconde approximation pour les écoulements transsoniques non visqueux, J. Mécanique, 5 (1966).

20. R. C. Lock, A Modification to the Method of Garabedian and Korn, Notes on Numerical Fluid Mechanics, Numerical Methods for the Computation of Inviscid Transonic Flows with Shock Waves, ed., A. Rizzi and H. Viviani, (Friedr. Vieweg & Sohn, Braunschweig/Wiesbaden, 1979), Vol. 3.
21. L. T. Chen, D. A. Caughey, and A. Verhoff, A Nearly Conformal Grid-Generation Method for Transonic Wing-Body Flowfield Calculation, AIAA Paper No. 82-108, (1982).
22. A. Jameson and D. A. Caughey, Numerical Calculation of the Transonic Flow Past a Swept Wing, ERDA Research and Development Report COO-3077-140, Mathematical Sciences, New York University, June 1977.
23. V. Schmitt and F. Charpin, Pressure Distributions on the ONERA-M6 Wing at Transonic Mach Numbers; in Experimental Data Base for Computer Program Assessment, AGARD-AR-138, May 1979.